Journal of Computational Physics 362 (2018) 69–94

Contents lists available at ScienceDirect

Journal of Computational Physics

www.elsevier.com/locate/jcp

Extended bounds limiter for high-order finite-volume schemes on unstructured meshes

Panagiotis Tsoutsanis

Centre for Computational Engineering Sciences, Cranfield University, Cranfield MK43 0AL, United Kingdom

ARTICLE INFO

Article history:
Received 7 November 2017
Received in revised form 29 January 2018
Accepted 5 February 2018
Available online 9 February 2018

Keywords:
MUSCL
Unstructured
Finite-volume
Limiter
Discontinuous

ABSTRACT

This paper explores the impact of the definition of the bounds of the limiter proposed by Michalak and Ollivier-Gooch in [56] (2009), for higher-order Monotone-Upstream Central Scheme for Conservation Laws (MUSCL) numerical schemes on unstructured meshes in the finite-volume (FV) framework. A new modification of the limiter is proposed where the bounds are redefined by utilising all the spatial information provided by all the elements in the reconstruction stencil. Numerical results obtained on smooth and discontinuous test problems of the Euler equations on unstructured meshes, highlight that the newly proposed extended bounds limiter exhibits superior performance in terms of accuracy and mesh sensitivity compared to the cell-based or vertex-based bounds implementations.

Crown Copyright © 2018 Published by Elsevier Inc. This is an open access article under the CC BY license (http://creativecommons.org/licenses/by/4.0/).

1. Introduction

Pursuit of accuracy has been one of the key-drivers for the development of novel numerical methods for the time-dependent Navier–Stokes equations, for the efficient application of Direct Numerical Simulation (DNS) and Large Eddy Simulation (LES) for structured and unstructured meshes. There are numerous approaches involving various frameworks that have tried to address the challenging task of obtaining a robust, efficient, high-order accurate, monotone and simple in implementation numerical scheme for unstructured meshes. State-of-the-art approaches span the finite volume (FV) [1–20, 48], the discontinuous Galerkin (DG) [15,21–29], the Spectral [30–37], and Flux Reconstruction (FR) [21,38–41] mathematical frameworks that have made novel efforts in trying to address these challenges for unstructured meshes.

How the high-order of spatial accuracy is achieved for these schemes varies, but the main objective is the same. This is detecting and eliminating spurious oscillations that can occur at flow regions of sharp gradients in any of the flow variables, and provide high-order of accuracy at smooth flow regions. Typical families of algorithms utilised to detect and eliminate the spurious oscillations include the MUSCL-Total Variation Diminishing (TVD) [42–44], the essentially non-oscillatory (ENO) [45] and weighted-ENO (WENO) [46], the Total Variation Bounding (TVB) [47] and the Multi-Dimensional Optimal Order Detection (MOOD) [48] scheme. The MOOD being different from the rest of the algorithms in the sense that it detects the maximum order of accuracy allowed without producing spurious oscillations and reduces the order of accuracy if some monotonicity conditions are not satisfied.

In this study, possible high-order extensions within the MUSCL framework for unstructured meshes are targeted. The main reason for using this framework is it's lower computational cost compared to ENO and WENO type of schemes, simplicity and robustness when low-quality of unstructured meshes are encountered. First limiter for FV schemes on unstructured meshes in 2D was proposed by Tilliayeva [49], which extended Kolgan's novel MUSCL approach [50,51] to arbitrary 2D cells.

E-mail address: panagiotis.tsoutsanis@cranfield.ac.uk.

https://doi.org/10.1016/j.jcp.2018.02.009
0021-9991/Crown Copyright © 2018 Published by Elsevier Inc. This is an open access article under the CC BY license (http://creativecommons.org/licenses/by/4.0/).

Barth and Jespersen [52] then presented a novel upwind scheme for unstructured grids by introducing a limiter that was acting on a linear reconstruction polynomial, and it was free of oscillations at regions of strong gradients that was widely used in 2D and 3D applications. The disadvantage with this limiter is that it uses non-differentiable functions that limit the convergence of non-linear problems to steady state. Venkatakrishnan [53] on the other hand introduced a modification to the limiter by making it differentiable. This way both the shortcomings such as achieving the second order accuracy and the convergence difficulties are overcome at least for smooth unstructured meshes.

The design of high-order limiters in the MUSCL framework is challenging for several reasons including obtaining differentiable functions, satisfying the bounds of the solution, dependency on the mesh quality, computational efficiency, simplicity and robustness. There have been numerous approaches that tried to address some of these aspects. Li and Ren [54] proposed a weighted biased averaging procedure (WBAP) limiter up to 4th-order of accuracy on unstructured meshes by employing non-linear weighting coefficients for the reconstruction. Liu and Zhang [55] proposed the distance weighted biased averaging procedure (DWBAP), which combines linear and non-linear weight coefficients and up to 4th-order of accuracy is obtained. Michalak and Ollivier-Gooch [56] proposed a limiting procedure for higher-order accurate unstructured finite-volume methods where a new differentiable function is used with a parameter controlling the balance between accuracy at non-uniform meshes and convergence properties. Excellent convergence and higher order accuracy at smooth regions and monotone behaviour were obtained with the Michalak and Ollivier-Gooch [56] (MOG).

In the present work the quest for a high-order limiter is going to be based on the Michalak and Ollivier-Gooch [56] limiter. This is because it is simple to implement and relies on the robust k-exact least-squares reconstruction. Although it is not parameter free it is less sensitive to the κ parameter introduced by Venkatakrishnan [53] to control monotonicity and accuracy balance as it has been reported by Michalak and Ollivier-Gooch [56] for a number of test problems.

However, there are two key issues that are encountered when developing and implementing limiters for higher-order schemes, that need to be considered. The first issue is associated with the distinction between vertex-based or cell-based approaches (not related to the formulation of the reconstruction itself or the implementation of the CFD code) for the establishment of the bounds of the reconstructed solution. Some approaches use the first-layer of neighbours (with the layer definition been different across different approaches), or the direct side neighbours, or the vertex neighbours of the considered cell. There are numerous limiters that due to the definition of their bounds they can exhibit significant variation in their performance when applied to a vertex-based or cell-based reconstruction. The second issue is associated with the definition of the bounds. The bounds are defined by the selected cells in the close spatial proximity that may differ from the total number of cells in the stencil. For 3rd-order and 4th-order schemes there is going to be a discrepancy between the number of cells in the stencil and the number of cells that are used for the definition of the bounds. This discrepancy itself could be important when designing high-order limiters, since for higher-order of accuracy eventually the bounds need to be violated or redefined. Therefore, by using more cells for defining the bounds of the solution, the bounds arising from fewer elements could be violated.

In the present work the impact of these two key issues are explored through new extensions of the high-order limiting procedure based on the Michalak and Ollivier-Gooch [56] limiter. A series of stringent test-problems of the Euler equations using unstructured meshes are considered, where the impact of the definition of bounds can be appreciated. Moreover, the extended limiter that utilises all the elements in the stencil as bounds, exhibits superior accuracy compared to the other implementations for all the test problems. The paper is organized as follows. Section 2 is dedicated to the generic framework used to describe the high-order finite-volume framework for unstructured meshes, the spatial discretisation, the implementation of the considered limiters, the fluxes and temporal discretisation. Numerous remarks are pointed out, for a series of algorithmic/formulation or implementation challenges faced. The numerical results obtained for the Euler equations are presented in Section 3 where the focus is on the accuracy and robustness of the limiter employed. The conclusions drawn from the present study are outlined in the last section.

2. General framework

The 2D unsteady compressible Euler equations are considered; written in compact form as:

$$\frac{\partial \mathbf{U}}{\partial t} + \nabla(\mathbf{F_c}(\mathbf{U})) = 0, \tag{1}$$

where $\mathbf{U} = \mathbf{U}(\mathbf{x}, t)$ is the vector of the unknown function, $\mathbf{x} = (x, y)$ denotes the coordinates of a point of the domain Ω, and $\mathbf{F_c}$ is the inviscid flux vector given by:

$$\begin{aligned} \mathbf{U} &= [\rho, \rho u, \rho v, E,]^T, \\ F_c^{\mathbf{x}} &= \left[\rho u, \rho u^2 + p, \rho uv, u(E+p)\right]^T, \\ F_c^{\mathbf{y}} &= \left[\rho v, \rho uv, \rho v^2 + p, v(E+p)\right]^T. \end{aligned} \tag{2}$$

In the above equations, ρ is the density; u, v are the velocity components in x, y Cartesian directions respectively. Calorically perfect gas is assumed where the total energy is computed according to the equation of state as $E = p/(\gamma - 1) + (1/2)\rho(u^2 + v^2)$, where p is the pressure, and the ratio of specific heats is set as $\gamma = 1.4$ unless otherwise stated.

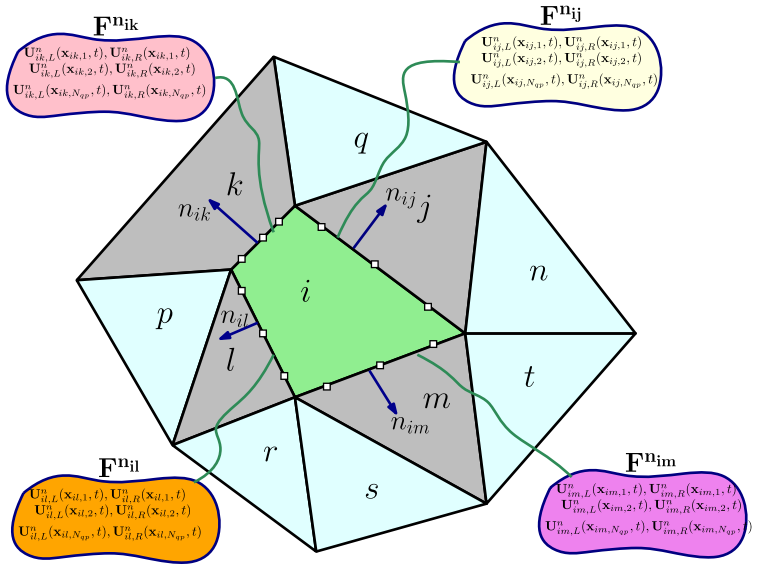


Fig. 1. Schematic of region around considered cell i, and it's direct side neighbours in grey colour, the corresponding normal vectors for each of it's sides, and the quadrature points at the edges in white colour.

The physical domain Ω in 2D consists of any combination of conforming quadrilateral and triangular elements of surface area S_i, indexed by a unique mono-index i. Integrating Eq. (1) over a mesh element using a high-order explicit finite-volume formulation the following equation is obtained:

$$\mathbf{U}_i^{n+1} = \mathbf{U}_i^n - \Delta t \frac{1}{|S_i|} \sum_{j=1}^{N_f} \sum_{\alpha=1}^{N_{qp}} \mathbf{F}^{\mathbf{n_{ij}}} \left(\mathbf{U}_{ij,L}^n(\mathbf{x}_{ij,\alpha}, t), \mathbf{U}_{ij,R}^n(\mathbf{x}_{ij,\alpha}, t) \right) \omega_\alpha |E_{ij}|, \tag{3}$$

where $\mathbf{U}_i$ are the volume averaged conserved variables, $\mathbf{F}^{\mathbf{n_{ij}}}$ is a numerical flux function in the direction normal to the cell interface between cell i and the neighbouring cell at the cell face j, N_f is the number of faces/sides per element, N_{qp} is the number of quadrature points used for approximating the line integrals, $|E_{ij}|$ is the length of the corresponding edge, $\mathbf{U}_{ij,L}^n(\mathbf{x}_\alpha, t)$ and $\mathbf{U}_{ij,R}^n(\mathbf{x}_\alpha, t)$ are the high-order approximation of the solution at the left (considered cell) and the right (neighbouring cell) of the cell interface respectively; finally α corresponds to different Gaussian integration points $\mathbf{x}_\alpha$ and weights ω_α over the edge as shown in Fig. 1.

The weights and distribution of the quadrature points depend upon the order of the Gaussian rule and in the present study a Gauss–Legendre quadrature is employed. The high-order approximation of the conserved vector for the intercell fluxes is obtained by a reconstruction process that employs cell-averaged data. The following sections describe the methodology adopted for space and time discretisation.

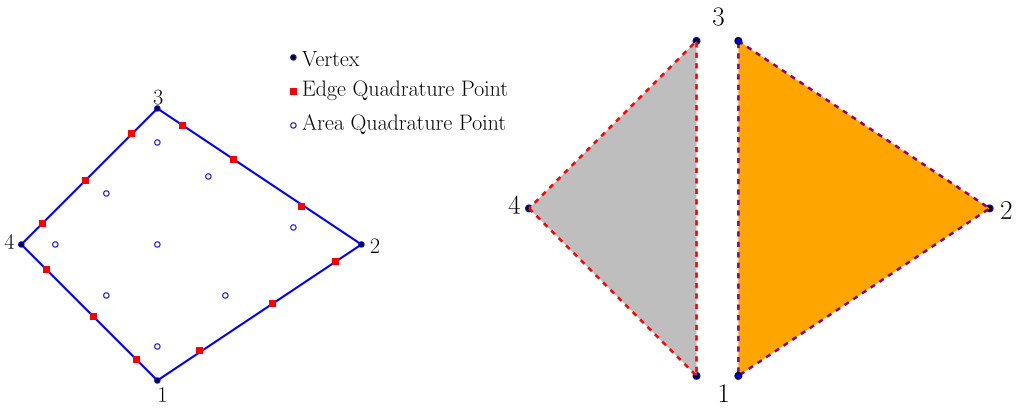
2.1. Spatial discretization

The main objective of the reconstruction process is to build a high-order polynomial $p_i(x, y)$ of arbitrary order r, for each considered element i that has the same average as a general quantity $\mathbf{U}_i$. This can be formulated as:

$$\mathbf{U}_i = \frac{1}{|S_i|} \int_{S_i} \mathbf{U}(x, y)\, dS = \frac{1}{|S_i|} \int_{S_i} p_i(x, y)\, dS. \tag{4}$$

The present reconstruction algorithm is based upon the approaches of [4,5,9], that has been successfully applied to smooth and discontinuous flow problems [8,57–63] and only key-components will be presented herein, and the reader is referred to [4,5,9] for further details.

For minimising the scaling effects that appear in grids consisting of elements of different sizes, many approaches exist including inverse-distance weighting, transformation to a reference coordinate system and column-scaling among others. Column scaling approach of Jalali and Ollivier-Gooch [64] deals with improving the condition number of least-squares systems by scaling the reconstruction matrix with the large entry of each column. Inverse distance-weighted least-squares reconstruction is reducing the influence of the elements farther away from the considered cell in the reconstruction process. For the present study the reconstruction is carried out in a transformed system of coordinates for improving the condition number of the system of equations similarly to [4,5,9,16,17,65]. The transformation is achieved by decomposing



(a) Schematic of a quadrilateral cell.

(b) Decomposition of the quadrilateral cell in two triangles for transformation to reference space, based on any of the two decomposed triangles.

Fig. 2. Schematic of quadrilateral cell and decomposition into triangles for transformation to reference space.

each element into triangular elements and using one of the decomposed triangular elements as the reference element for transforming to the new system of coordinates as shown in Fig. 2. It must be stressed that this transformation is only computed once at the initialisation phase of our simulation since the mesh does not change with time for the present study, and is intended for performing reconstruction in a reference space.

Let $\mathbf{v}_{ij},\ j=1,2,\dots J_i$ be the vertices of the considered general element. By decomposing non-triangular elements into triangles and choosing one of them with $\mathbf{w}_1=(x_1,y_1)$, $\mathbf{w}_2=(x_2,y_2)$, $\mathbf{w}_3=(x_3,y_3)$, being it's three vertices. These vertices are always one of the $\mathbf{v}_{ij}$ ones. The transformation from the Cartesian coordinates x, y into a reference space ξ,η is given by the following equations:

$$\begin{pmatrix} x \\ y \end{pmatrix} = \begin{pmatrix} x_1 \\ y_1 \end{pmatrix} + J \cdot \begin{pmatrix} \xi \\ \eta \end{pmatrix}, \tag{5}$$

with the Jacobian matrix given by:

$$J = \begin{bmatrix} x_2 - x_1 & x_3 - x_1 \\ y_2 - y_1 & y_3 - y_1 \end{bmatrix}. \tag{6}$$

Using an inverse mapping the element S_i can be transformed to the element S_i' in the reference co-ordinate system as:

$$\mathbf{v}'_{ij} = J^{-1} \cdot \left(\mathbf{v}_{ij} - \mathbf{w}_1\right), \quad j=1,2,\dots J_i, \tag{7}$$

and the spatial average of the conserved variable $\mathbf{U}_i$ does not change during transformation

$$\mathbf{U}_i = \frac{1}{|S_i|}\int_{S_i} \mathbf{U}(x,y)\, dS \equiv \frac{1}{|S_i'|}\int_{S_i'} \mathbf{U}(\xi,\eta)\, d\xi d\eta. \tag{8}$$

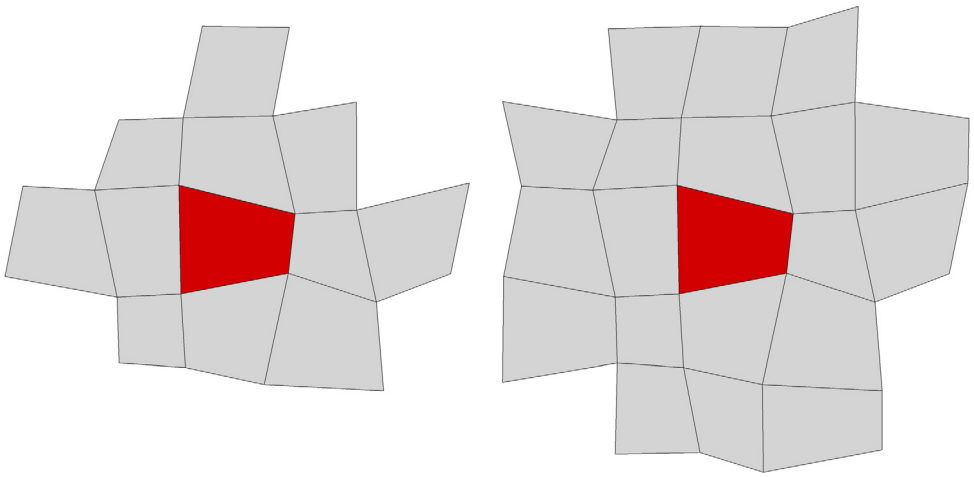
To perform the reconstruction on the target element S_i, the central reconstruction stencil is formed $\mathcal{S}$ by recursively adding neighbouring elements, consisting of $M+1$ elements, including the target element S_i as shown in Fig. 3,

$$\mathcal{S} = \bigcup_{m=0}^{M} S_m, \tag{9}$$

where the index m refers to the local numbering of the elements in the stencil, with the element with index 0 being the considered cell i.

Stencil selection strategies is a challenging task when dealing with high-order methods on unstructured meshes since there is a variation of the size and quality of the elements that can play a crucial role in the reconstruction accuracy, robustness and computational cost.

Remark 1. The stencil size can be measured in terms of number of cells included in it. Their number is proportional to the computational requirements, robustness and inversely proportional to the accuracy, since compact stencils (with fewer elements) can achieve higher accuracy as opposed to stencils with more elements. Typical example of approaches include adding a single layer of neighbours for every increment of the spatial order of accuracy [64], and adding neighbours in the



(a) 3rd-order stencil (b) 4th-order stencil

Fig. 3. Examples of central stencils with the considered cell in red colour. (For interpretation of the references to colour in this figure legend, the reader is referred to the web version of this article.)

stencil until a target condition number for the matrix of the linear system has been achieved [2,48] although there should be stop criteria in place to prevent the stencil growing too much in size.

Therefore algorithms that use criteria such as adding the closest elements to the considered cell might thrive in uniform meshes since they can result in quite compact stencils, but they will fail in meshes of poor quality since they can result in stencil elements aligned in one coordinate direction that can impair the robustness of the multi-dimensional reconstruction. Hence, there is a plethora of strategies that could be considered to build the "ideal" stencil selection algorithm that adapts based on the quality of the spatial information available and computational budgets.

Remark 2. Investigating various stencil selection algorithms is beyond the scope of the present paper although it is an interesting aspect that could be pursued in the future, and for the sake of robustness more cells are involved in the stencil than the number of equations $K = \frac{1}{2}(r+1)(r+2)-1$. So similarly to [2,4,5,9,14,16], the number of employed cells including the considered cell are, 5 cells for $r = 1$, 12 cells for $r = 2$ and 20 cells for $r = 3$. The selection process is based on firstly adding the direct side neighbours, and then recursively adding neighbours of neighbours until the required number of elements is reached.

The considered cell and it's corresponding stencil is transformed in the reference space as shown in Fig. 4,

$$\mathcal{S}' = \bigcup_{m=0}^{M} S'_m, \tag{10}$$

and the rth order reconstruction polynomial at the transformed cell S'_0 is sought as an expansion over local polynomial basis functions $\lambda_k(\xi,\eta)$ given by:

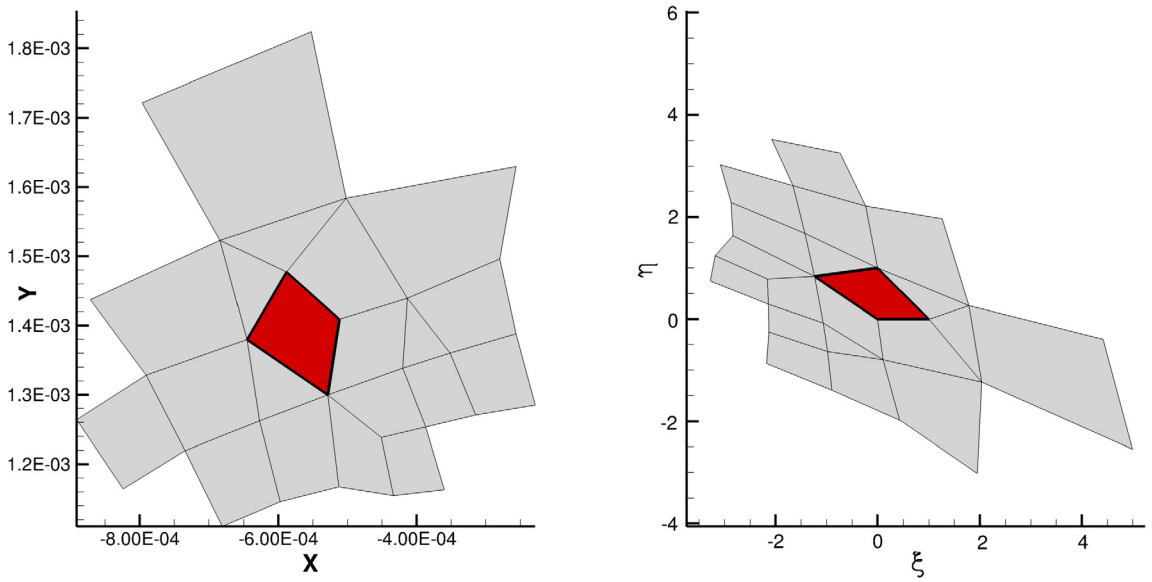
$$p(\xi,\eta) = \sum_{k=0}^{K} a_k \lambda_k(\xi,\eta) = \mathbf{U}_0 + \sum_{k=1}^{K} a_k \lambda_k(\xi,\eta), \tag{11}$$

where $\mathbf{U}_0$ corresponds to the vector of conserved variables at the considered cell i, and ξ,η are the coordinates in the reference system. a_k are the degrees of freedom and the upper index in the summation of expansion K corresponds to the number of the degrees of freedom.

To find the unknown degrees of freedom a_k for each cell m from the stencil the cell average of the reconstruction polynomial $p(\xi,\eta)$ must be equal to the cell average of the solution $\mathbf{U}_m$:

$$\int_{S'_m} p(\xi,\eta)\, d\xi d\eta = |S'_m|\mathbf{U}_0 + \sum_{k=1}^{K} \int_{S'_m} a_k \lambda_k \, d\xi d\eta = |S'_m|\mathbf{U}_m, \quad m = 1,\ldots,M. \tag{12}$$

Where S'_m is the surface area of the cell m in the stencil in the transformed coordinate system. Since for general cells the transformation in a unit quadrilateral cell cannot be guaranteed, the basis functions λ_k used should satisfy the constraint of



(a) Central stencil in physical space.

(b) Central stencil in reference space.

Fig. 4. Examples of central stencils in physical space and (x, y) coordinates and in transformed reference space and (ξ, η) coordinates with the considered cell illustrated in red colour. (For interpretation of the references to colour in this figure legend, the reader is referred to the web version of this article.)

equation (4) irrespective of the values of degrees of freedom. The basis functions λ_k for all the elements in the stencil are defined as follows:

$$\lambda_k(\xi,\eta) \equiv \psi_k(\xi,\eta) - \frac{1}{|S_0'|}\int_{S_0'} \psi_k \, d\xi d\eta \quad k = 1, 2, \ldots, K, \tag{13}$$

where S_0' is the surface area of the considered cell i, in the transformed coordinate system, and in the present study ψ_k are Legendre polynomials basis functions. Denoting the integrals of the basis function k over the cell m in the stencil, and the vector of right-hand side by A_{mk} and b respectively as given by

$$A_{mk} = \int_{S_m'} \lambda_k \, d\xi d\eta, \quad b_m = |S_m'|(\mathbf{U}_m - \mathbf{U}_0),$$

the equations for degrees of freedom a_k can be rewritten in a matrix form as:

$$\sum_{k=1}^{K} A_{mk} a_k = b_m, \quad m = 1, 2, \ldots M. \tag{14}$$

The complete linear system is given by:

$$\begin{bmatrix} A_{1,1}(\xi,\eta) & A_{1,2}(\xi,\eta) & A_{1,3}(\xi,\eta) & \cdots & A_{1,K}(\xi,\eta) \\ A_{2,1}(\xi,\eta) & A_{2,2}(\xi,\eta) & A_{2,3}(\xi,\eta) & \cdots & A_{2,K}(\xi,\eta) \\ \vdots & \vdots & \vdots & \cdots & \vdots \\ A_{M,1}(\xi,\eta) & A_{M,2}(\xi,\eta) & A_{M,3}(\xi,\eta) & \cdots & A_{M,K}(\xi,\eta) \end{bmatrix} \begin{bmatrix} a_1 \\ a_2 \\ \vdots \\ a_K \end{bmatrix} = \begin{bmatrix} |S_1'|(\mathbf{U}_1 - \mathbf{U}_0) \\ |S_2'|(\mathbf{U}_2 - \mathbf{U}_0) \\ \vdots \\ |S_M'|(\mathbf{U}_M - \mathbf{U}_0) \end{bmatrix}. \tag{15}$$

The matrix A_{mk} is purely based on the geometry of the elements in the stencils, which remains unchanged for the present study, while the information on the right-hand vector b_m is dependent upon the solution, and the surface area of each of the element in the stencil in the transformed coordinate system. The matrix $A_{km}^T A_{mk}$, is invertible and the equation (14), can be rewritten in the following form:

$$a_k = \left(A_{km}^T A_{mk}\right)^{-1} A_{km}^T b_m = A_{km}^{\dagger} b_m, \tag{16}$$

where the matrix $A_{km}^{\dagger}$ corresponds to the Moore–Penrose pseudo-inverse of A_{mk}. The polynomial coefficients are therefore obtained through a matrix vector multiplication of $A_{km}^{\dagger}$ with b_m. In the present study a QR decomposition based on

Householder transformation [66] is used, where the pseudo-inverse is decomposed in the following manner in an orthogonal matrix Q and an upper triangular one R, and the inverse of $R^T R$ is obtained by a forward-substitution followed by a backward-substitution.

$$A^{\dagger}_{km} = \left((Q\,R)^T (Q\,R) \right)^{-1} A^T_{km} = \left(R^T R \right)^{-1} A^T_{km} \tag{17}$$

The main memory requirements of the present least-squares reconstruction is the associated storage of the pseudo-inverse matrix $A^{\dagger}_{km}$, that is only computed once at the preprocessing stage of the simulation.

2.2. MUSCL

In the MUSCL framework employed in this work the high-order variation of the solution within every cell is approximated by the corresponding polynomial, whose degrees of freedom a_k are computed during the least-squares reconstruction process by incorporating information from the entire central stencil as shown in Fig. 3. The scheme can be written as:

$$\mathbf{U}_{ij,\alpha} = \mathbf{U}_i + \phi_i \cdot \sum_{k=1}^{K} a_k \lambda_k(\xi_a, \eta_a), \tag{18}$$

where $\mathbf{U}_{ij,\alpha}$ is the extrapolated reconstructed solution at face j, and at quadrature point α, $\mathbf{U}_i$ is the value for the conserved variable of element i, and (ξ_a, η_a) are the coordinates of the quadrature point at the ij edge. All polynomials, for all the faces and for all the quadrature points are then limited by the limiter ϕ_i which is valid for cell i to prevent any spurious oscillations from contaminating the solution.

2.2.1. Barth and Jespersen limiter (BJ)

One of the first limiters that has been widely used for unstructured meshes is the slope limiter of Barth and Jespersen [52]. Although this limiter is not considered in the present work due to it's non-differentiable nature and limited application for high-order schemes, elements of this limiter are going to be used as a building block for high-order limiters and therefore it's key characteristics are outlined. The design of this slope limiter requires the minimum and maximum values from the stencil formed by the considered cell i and the direct side neighbours:

$$\mathbf{U}^{min}_i = \min(\mathbf{U}_l : l = 1, .., L) \;\; and \;\; \mathbf{U}^{max}_i = \max(\mathbf{U}_l : l = 1, .., L), \tag{19}$$

where $l = 1, .., L$; L is the local numbering for the cell i and it's direct-side neighbours, where $l = 1$ corresponds to the cell i. The limiter seeks the minimum value of the slope limiter for all the direct-side neighbours,and all the quadrature points α that satisfy the following conditions:

$$\phi_i = \min(\phi_{il,a}) \qquad l \in [1, L], \qquad \alpha \in [1, N_{qp}]. \tag{20}$$

Where $\phi_{il,\alpha}$ corresponds to the slope limiter value at side l and quadrature point α for cell i. Then, the limiting function is applied, composed by three different states according to the difference of the unlimited reconstructed value $\mathbf{U}_{il,\alpha}$ at the quadrature points of the considered element $\mathbf{U}_{(i,l,\alpha)}$, the minimum $\mathbf{U}^{min}_i$ and maximum $\mathbf{U}^{max}_i$ values from the direct-side neighbours, yielding:

$$\phi_{il,\alpha} = \begin{cases} \min\left(1, \dfrac{\mathbf{U}^{max}_i - \mathbf{U}_i}{\mathbf{U}_{il,\alpha} - \mathbf{U}_i}\right), & \text{if } \mathbf{U}_{il,\alpha} - \mathbf{U}_i > 0 \\ \min\left(1, \dfrac{\mathbf{U}^{min}_i - \mathbf{U}_i}{\mathbf{U}_{il,\alpha} - \mathbf{U}_i}\right), & \text{if } \mathbf{U}_{il,\alpha} - \mathbf{U}_i < 0 \\ 1, & \text{if } \mathbf{U}_{il,\alpha} - \mathbf{U}_i = 0 \end{cases} \tag{21}$$

2.2.2. Michalak and Ollivier-Gooch limiter (MOG)

The high-order limiter that is going to be used as the reference in the present work is the Michalak and Ollivier-Gooch [56] limiter, and expansions of these limiter are going to be explored. Therefore, the key-details of this limiter are outlined. For achieving the accuracy of the higher order schemes, Michalak and Ollivier-Gooch [56] proposed a new function $\widetilde{min}(1, y)$ which replaces the minimum function of Barth and Jespersen slope limiter [52]. Similar to Venkatakrishnan's [53] function this needs to be completely differentiable at all points and at the same time contained within the limit $min(1, y)$. An additional requirement is that this function should have an exact value of 1 for all the range of values $y \geq y_t$, where $1 < y_t < 2$ represents a threshold value. This function has the following form:

$$\widetilde{min}(1, y) = \begin{cases} P(y) & y < y_t \\ 1 & y \geq y_t \end{cases} \tag{22}$$

where $P(y)$ is a polynomial which satisfies the following criteria:

$$\begin{aligned} &P|_0 = 0, \quad P|_{y_t} = 1, \\ &\tfrac{dP}{dy}|_0 = 1, \quad \tfrac{dP}{dy}|_{y_t} = 0, \\ &P(y) \leq min(1, y) \quad y \in [0, y_t]. \end{aligned} \tag{23}$$

The resulting polynomial for $y_t = 1.50$ is given by the equation:

$$P(y) = \frac{-4}{27}(y^3) + y, \quad y_t = 1.50. \tag{24}$$

The choice of y_t is basically a compromise between maintaining a good accuracy and convergence properties on non-uniform grids and dictates the degree of non-uniformity that can be accommodated. In general smaller values of y_t are less likely to activate the limiter but increases its non-differentiability. Also, Michalak and Gooch [56] suggests that in order to maintain higher order accuracy it is necessary to deactivate the limiter in the smooth regions. Similar to the Venkatakrishnan limiter [53], the limiters are deactivated when the local solution variation is $O(\Delta x^2)$ or even smaller. Thus the action of limiter is deactivated under the following criteria:

$$\delta \mathbf{U} \equiv \delta \mathbf{U}_i^{max} - \delta \mathbf{U}_i^{min} < (\kappa \Delta x)^{\frac{3}{2}}, \tag{25}$$

where κ is a tunable parameter. Using a simple switch can worsen the convergence therefore to maintain differentiability a new modified limiter was utilised $\tilde{\phi}_i$ as follows:

$$\tilde{\phi}_i = \tilde{\sigma}_i + \phi_i(1 - \tilde{\sigma}_i), \tag{26}$$

where ϕ_i is the limiter value calculated as mentioned in equation (21) and is applied to all the degrees of freedom of the polynomial as seen in equation (18). The value of $\tilde{\sigma}_i$ is used as a switch in deactivating the limiter in the smooth region and its function is defined as:

$$\tilde{\sigma}_i = \begin{cases} 1 & \delta \mathbf{U}^2 \leq (\kappa \Delta x)^3 \\ S(\frac{\delta \mathbf{U}^2 - (\kappa \Delta x)^3}{(\kappa \Delta x)^3}) & (\kappa \Delta x)^3 < \delta \mathbf{U}^2 < 2(\kappa \Delta x)^3 \\ 0 & \delta \mathbf{U}^2 \geq (\kappa \Delta x)^3 \end{cases} \tag{27}$$

Where $S = 2y^3 - 3y^2 + 1$. Though this limiter deactivation looks similar to that of (VK) limiter, limiting actions are different between these two. The value of ϵ^2 as used in the (VK) limiter modifies the limiting value in all cases and increasing the value of κ causes larger overshoots in the solution especially at shock discontinuities. In this modified limiter the transition function is exactly 1, at regions of strong gradients, and the limiter achieves monotonicity regardless of κ, hence this modified limiter as proposed by Michalak and Ollivier-Gooch [56] is less sensitive to κ. For all the studies in the present work a $\kappa = 5$ is employed.

Remark 3. The key-elements that can lead to confusion when implementing a limiter such as the Michalak and Ollivier-Gooch [56] lies in the fact that the maximum and minimum bounds of the solution are determined by the immediate neighbours, similarly to Barth and Jespersen limiter [52] and the MOOD scheme of Diot et al. [2]. Some of the questions that arise from this are outlined below:

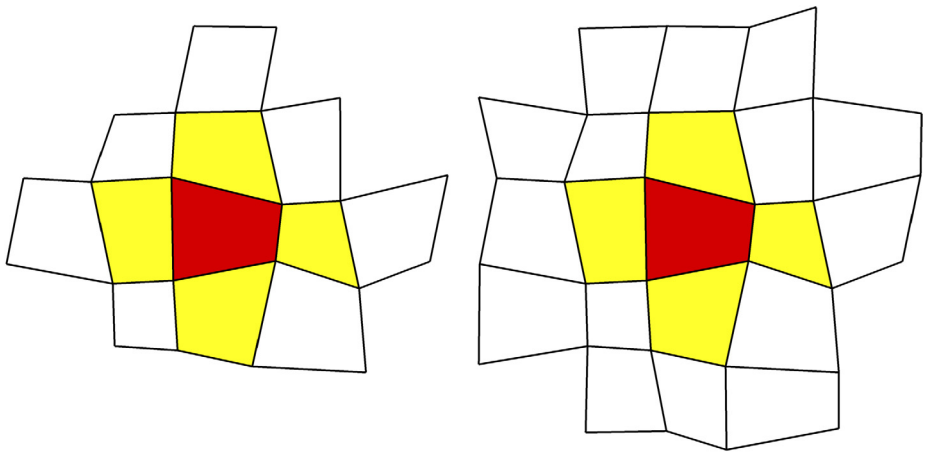
1. Vertex-based neighbours, or direct-side neighbours?
2. What happens when the number of vertex-based neighbours is greater that the number of stencil elements required, which can occur for meshes of poor quality?
3. Can the definition of this neighbourhood for establishing the bounds of the solution have an impact on the performance of the limiter?

In this paper, possible extensions of the limiter are pursued, by exploring the answers to the above questions. Following the work and definition [52], the subject MOG limiter is going to be implemented by using the direct-side neighbours of the considered cell, as the elements that bound the solution as shown in Fig. 5.

2.2.3. Michalak and Ollivier-Gooch limiter vertex based (MOGV)

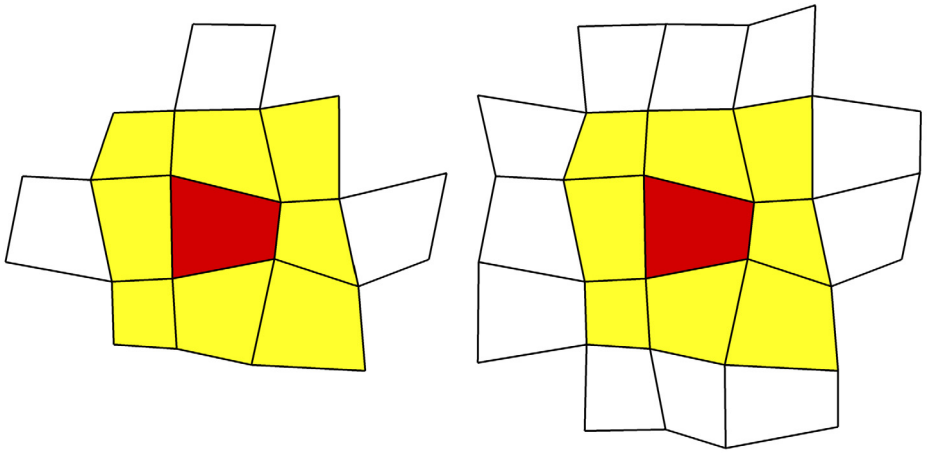
The first modification or variation in the implementation of the MOG limiter, is to ensure that all the vertex-based neighbouring elements are used to obtain the solution bounds. However, this has the following consequences:

1. For the 2nd-order implementation of this limiter, more than 5 cells will be used for bounding the solution which was the initial number of cells already employed in the stencil selection algorithm, therefore ending up with more elements in the stencil.



(a) MOG3 (b) MOG4

Fig. 5. Stencils for 3rd and 4th-order MOG limiter, the $\mathcal{M}in$ and $\mathcal{M}ax$ bounds are obtained from the yellow coloured elements and the considered cell in red colour. (For interpretation of the references to colour in this figure legend, the reader is referred to the web version of this article.)



(a) MOGV3 (b) MOGV4

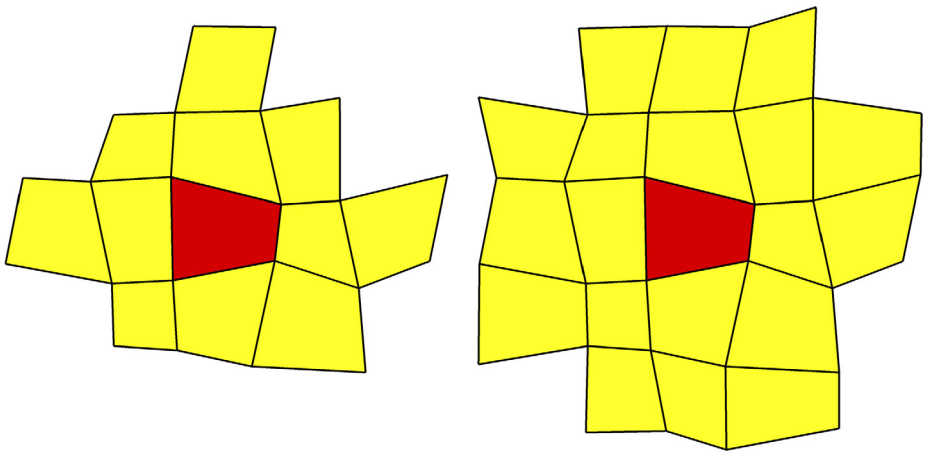
Fig. 6. Stencils for 3rd and 4th-order MOGV limiter, the $\mathcal{M}in$ and $\mathcal{M}ax$ bounds are obtained from the yellow coloured elements and the considered cell in red colour. (For interpretation of the references to colour in this figure legend, the reader is referred to the web version of this article.)

2. The stencil selection algorithm is modified to ensure that it uses all the vertex side neighbours for all spatial orders, and recursively add as many elements needed to reach the number of elements required.
3. For poor quality of meshes a vertex based stencil selection algorithm can result in significant more elements than a cell based stencil selection algorithm.
4. For meshes of good quality for 3rd-order and 4th-order schemes the number of vertex-based neighbours is always smaller than the total number of elements in the stencil.

The implementation of the present vertex-based neighbours is used for the limiting purposes only rather than changing the entire implementation of the used UCNS3D code [4,5,8,57–60] to vertex-based. UCNS3D is a parallel 2D and 3D unstructured CFD research code written in Fortran, and uses the cell-centred finite-volume framework and WENO and MUSCL schemes for steady-state and unsteady flow problems. This subject modification/variation of the MOG limiter using the vertex-based neighbours as the elements that bound the solution is going to be labelled (MOGV) as it can be seen in Fig. 6.

2.2.4. Michalak and Ollivier-Gooch limiter extended bounds (MOGE)

The MOG and MOGV limiters contain all the required ingredients to enable high-order of spatial accuracy, for uniform grids in principle. However, for more realistic unstructured meshes there are additional parameters that can prohibit the scheme from achieving it's designed order of accuracy. One key parameter is that the geometry of the unstructured mesh and the resulting condition number of the least-squares system reconstruction can activate the limiter itself. The other parameter is the mismatch between the stencil elements used for the reconstruction, and the elements that dictate the



(a) MOGE3 (b) MOGE4

Fig. 7. Stencils for 3rd and 4th-order MOGE limiter, the $\mathcal{M}in$ and $\mathcal{M}ax$ bounds are obtained from the yellow coloured elements and the considered cell in red colour. (For interpretation of the references to colour in this figure legend, the reader is referred to the web version of this article.)

$\mathcal{M}in$ and $\mathcal{M}ax$ bounds of the solution for smooth and discontinuous flow regions. To give a better perspective of this parameter consider the following:

1. Assume that the unlimited reconstructed solution of a smooth function in a good quality mesh is accurate and does not produce any oscillations
2. This unlimited reconstructed solution might be out of the bounds established from the direct-side neighbours and the considered cell.
3. By applying a limiter using these bounds the reconstructed solution will be unnecessarily limited.

Remark 4. It must be stressed that for obtaining higher-order of accuracy, eventually the **bounds** must be violated. The definition of the **bounds** associated with these type of limiters can be redefined. Therefore the development of a scheme that can be considered either a **bound-violating**, or a limiter with **wider-bounds** is pursued.

In smooth flow regions, a limiter should be completely deactivated since the unlimited reconstruction can produce a high-order accurate solution without any oscillations. Therefore, in principle the unlimited reconstruction should provide boundary extrapolated reconstructed solutions at the quadrature points of the considered cell that lie within the values of all the elements in the stencil in smooth flow regions. Hence, for smooth flow regions the bounds provided by the direct side neighbours, or the vertex neighbours have a narrower range of values allowed. Furthermore, when the unlimited reconstructed solution is out of these bounds, the limiter function is controlled by the threshold value y_t, and for meshes of poor quality the limiting applied could prove to be excessive and more dependent upon the mesh quality.

For discontinuous flow regions, even if one element in the stencil neighbourhood lies in a discontinuous region it can produce oscillations in the unlimited reconstructed solution, especially if the mesh quality is poor and consequently the condition number of the linear system is relatively large. This will in turn activate the limiter although the bounds are determined by all the elements included in the stencil.

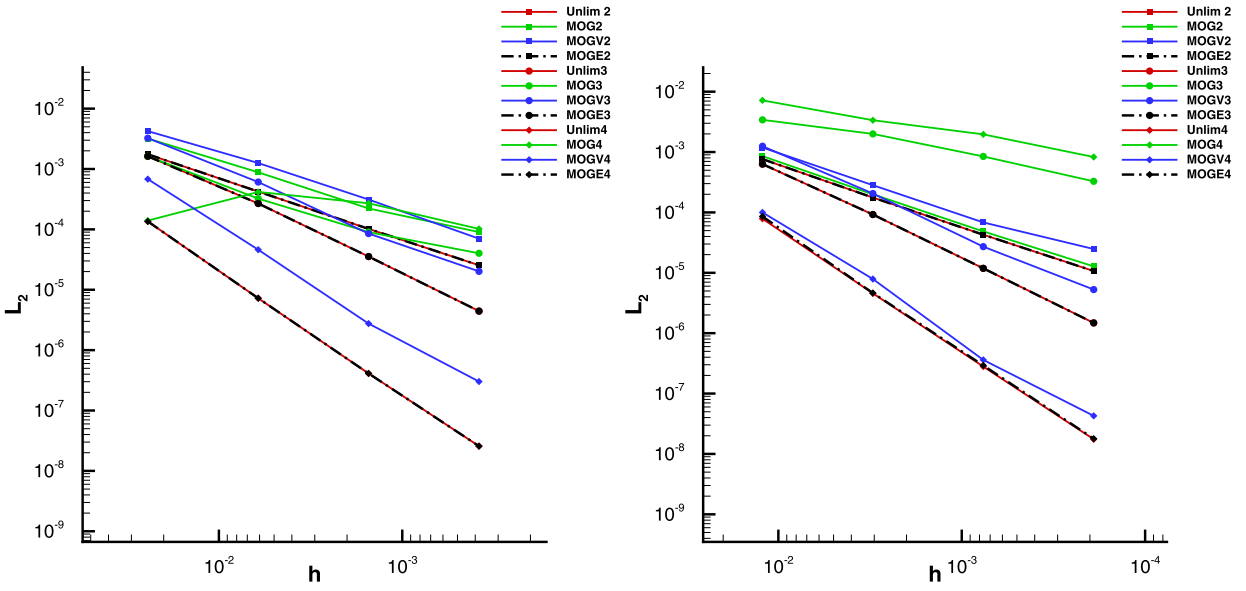
Remark 5. For this modified version of the MOG limiter, reducing the threshold value y_t for reducing the activation of the limiter at non-uniform meshes would result in increased non-differentiability of the limiter which is undesirable. Hence, by simply obtaining the $\mathcal{M}in$ and $\mathcal{M}ax$ bounds of the solution from all the elements in the stencil, in principle the performance of the limiter would become less sensitive to the grid quality.

The minimum and maximum values from the all the elements in the stencil including the considered cell i are considered:

$$\mathbf{U}_i^{min} = \min(\mathbf{U}_m : m = 1, .., M) \text{ and } \mathbf{U}_i^{max} = \max(\mathbf{U}_m : m = 1, .., M), \tag{28}$$

where $m = 1, .., M$; M is the local numbering for the cell i and it's stencil elements, where $m = 1$ corresponds to the cell i.

This limiter with the extended bounds is labelled (MOGE) and the stencil elements used for a third-order and fourth order scheme, can be seen in Fig. 7.



(a) Quadrilateral Meshes (b) Triangular Meshes

Fig. 8. L^2 convergence curves obtained with various numerical schemes on quadrilateral and triangular meshes for the 2D vortex evolution problem at $t = 10$. (For interpretation of the colours in this figure, the reader is referred to the web version of this article.)

2.3. Fluxes approximation and temporal discretisation

For the evaluation of the intercell numerical flux function $\mathbf{F}^{\mathbf{n}_{ij}}$ the approximate HLLC (Harten–Lax–van Leer-Contact) Riemann solver of Toro [67] is employed. For ensuring that the pressure and density remain positive through the reconstruction the positivity condition of [68] is used where the reconstructed values of density and pressure for each Gaussian quadrature points (α) and for all the faces l must satisfy the following:

$$|\rho_{il,\alpha} - \rho_i| < 0.8\rho_i \quad \text{and} \quad |p_{il,\alpha} - p_i| < 0.8p_i. \tag{29}$$

If the condition (29) is not satisfied for any of the Gaussian quadrature point then the order of the accuracy for the cell is reduced by one order until the condition is satisfied. The solution is advanced in time by the explicit Strong Stability Preserving (SSP) Runge–Kutta 4th-order method of Spiteri and Ruuth [69] which is stable for $CFL \approx 1.50$, with a constant wave speed estimate during the 5 stages, and a CFL of 1.3 is used for all the test-cases in the present study, unless otherwise stated. For all the test problems involved the initial condition is approximated with a 7th-order Gaussian quadrature rule, to ensure that the initial condition is of high-accuracy, and during the simulation the volume/surface/line integrals are approximated by Gaussian quadrature rule suitable for the order of polynomial employed.

3. Numerical results

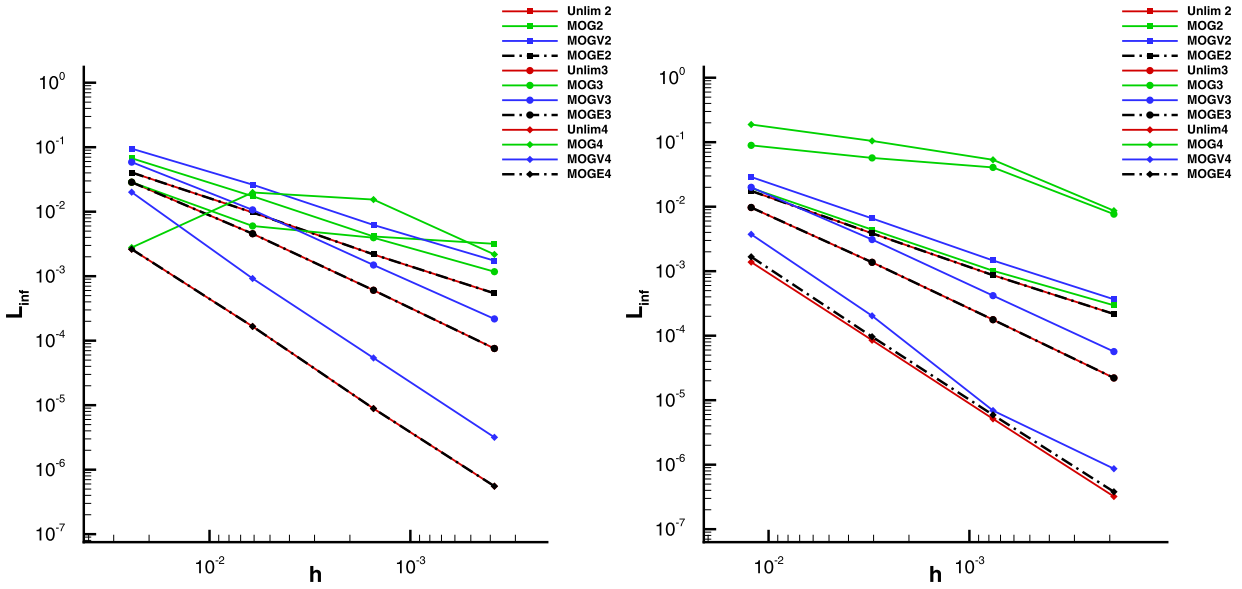
3.1. 2D vortex evolution

The 2D vortex evolution test problem presented by Balsara and Shu [70] is used where an isentropic vortex propagates at supersonic Mach number at 45° across the domain. The computational domain is given by $[0, 10] \times [0, 10]$ with periodic boundary conditions applied on all sides. The unperturbed domain has an initial condition $(\rho, u, v, p) = (1, 1, 1, 1)$, where temperature and density are defined as $T = p/\rho$, and $S = p/r^{\gamma}$ the adiabatic gas constant $\gamma = 1.4$ and the vortex perturbations are given by:

$$\delta T = -\frac{(\gamma - 1)\,\epsilon^2}{8\gamma\pi^2} e^{(1-r^2)}, \qquad (\delta u, \delta v) = \frac{\epsilon}{2\pi} e^{0.5(1-r^2)} \left(-(y-5), (x-5)\right). \tag{30}$$

The vortex strength $\epsilon = 5$ and adiabatic gas constant $\gamma = 1.4$. The e_{L^2} and the e_{L^∞} errors are computed as follows:

$$e_{L^2} = \sqrt{\frac{\sum_i \int_{\Omega_i} \left(\mathbf{U}_e\left(x, t_f\right) - \mathbf{U}_c\left(x, t_f\right)\right)^2 dV}{\sum_i |\Omega_i|}}, \tag{31}$$



(a) Quadrilateral Meshes (b) Triangular Meshes

Fig. 9. L^{∞} convergence curves obtained with various numerical schemes on quadrilateral and triangular meshes for the 2D vortex evolution problem at $t = 10$. (For interpretation of the colours in this figure, the reader is referred to the web version of this article.)

$$e_{L^{\infty}} = \mathcal{M}ax \left| \left(\mathbf{U}_e \left(x, t_f \right) - \mathbf{U}_c \left(x, t_f \right) \right) \right|, \tag{32}$$

where $\mathbf{U}_c \left(x, t_f \right)$ and $\mathbf{U}_e \left(x, t_f \right)$ are the computed and exact solutions at the end of the simulation t_f. The exact solution $\mathbf{U}_e \left(x, t_f \right)$ being given by the initial condition itself at t_0. Two types of unstructured meshes a quadrilateral and triangular types are used for this test problem of 64, 128, 256 and 512 nodes per side resolution, and the simulation is run for a time of $t_f = 10$. From the L^2 and L^{∞} convergence curves at Fig. 8 and Fig. 9 it can be noticed that all the unlimited schemes achieve their designed order of accuracy for both mesh types. As expected the MOGE version of the limiter is the one that has the closest agreement with it's equivalent unlimited scheme, since the reconstructed solution is within the bounded values of all the elements in the stencil, therefore the limiter is not activated at all. The vertex based MOGV limiter is not as accurate as the unlimited scheme, since the fact that there is a discrepancy between the number of elements used for bounding the reconstructed solution and the total number of elements, this results in the limiter being mistakenly activated especially. Lastly, the MOG limiter is the one that is the most sensitive in terms of being activated, due to the exaggerated difference between bounding elements and stencil elements, which is worse for triangular meshes. For comparing the accuracy and computational cost of all the schemes, the WENO method of Tsoutsanis et al. [4,5] has also been utilised for this test problem. From the results of Table 1 and Table 2, it can be seen that the WENO method of same order of accuracy is as accurate as the MOGE and the unlimited scheme for this test problem. However, the computational cost is increased by (60% to 300%) compared to the MOGE scheme due to the additional reconstruction stencils and the overheads associated with them. In general the fourth order schemes reduce the e_{L^2} two to three orders of magnitude more than a second order scheme for the same computational cost. It has to be noted that all the CPU measurements have been taken at the Hazelhen High Performance Computing Cluster consisting of Intel Haswell E5-2680 v3 CPUs with 24 cores per node, and all the CPU times are expressed in units of $(cores \times time(sec))$.

3.2. Shu–Osher problem

A widely used benchmark for high-order schemes is the Shu–Osher [71] problem where the interaction between a shock wave and an entropy wave takes place. The computational domain is $[-5, 5] \times [-0.1, 0.1]$, with periodic boundary conditions in y-axis, a supersonic inflow and outflow on the left and right side of the domain respectively. The initial profile consists of a shock wave $(\rho, u, v, p) = (3.857143, 2.629369, 0, 10.333333)$ on the left when $x < -4$ and an entropy wave in the rest of the domain $(\rho, u, v, p) = (1 + 0.2sin(5x), 0, 0, 1)$.

Two unstructured meshes of triangular elements with 128 and 256 nodes for the top and bottom sides with approximately 16,000 and 52,000 elements. The reference solution is computed with an one-dimensional Euler equations on 10,000 grid points using a WENO-5th order scheme. The calculation is run until $t = 1.8$. From the density distribution and limiting function ϕ plots for th 4th-order limiter of the fine mesh at Fig. 10 it can be seen that the MOG limiter is being activated in more regions that the MOGV and MOGE limiters where they are activated in the expected regions of sharp-gradients.

Table 1
L^2 and L^∞ errors and convergence rates, and CPU time ($cores \times time(sec)$) for the 2D vortex evolution problem obtained with various orders of accuracy with the unlimited, MOG, MOGV, MOGE and WENO scheme at the final time of $t = 10$ on quadrilateral meshes.

Mesh points	Unlimited $\mathcal{O}=2$					Unlimited $\mathcal{O}=3$					Unlimited $\mathcal{O}=4$				
	e_{L^2}	$\mathcal{O}_{L^2}$	e_{L^∞}	$\mathcal{O}_{L^\infty}$	CPU	e_{L^2}	$\mathcal{O}_{L^2}$	e_{L^∞}	$\mathcal{O}_{L^\infty}$	CPU	e_{L^2}	$\mathcal{O}_{L^2}$	e_{L^∞}	$\mathcal{O}_{L^\infty}$	CPU
64^2	1.752E−03	–	4.048E−02	–	7.51	1.625E−03	–	2.864E−02	–	12.64	1.353E−04	–	2.618E−03	–	21.77
128^2	4.231E−04	2.05	9.738E−03	2.05	44.89	2.685E−04	2.59	4.551E−03	2.65	97.42	7.242E−06	4.22	1.661E−04	3.97	159.60
256^2	1.018E−04	2.05	2.173E−03	2.16	281.36	3.546E−05	2.92	6.052E−04	2.91	723.41	4.109E−07	4.13	8.862E−06	4.22	1167.72
512^2	2.545E−05	2.00	5.425E−04	2.00	1230.62	4.433E−06	2.99	7.565E−05	3.00	4579.23	2.571E−08	4.00	5.540E−07	3.99	8285.36

Mesh points	MOG $\mathcal{O}=2$					MOG $\mathcal{O}=3$					MOG $\mathcal{O}=4$				
	e_{L^2}	$\mathcal{O}_{L^2}$	e_{L^∞}	$\mathcal{O}_{L^\infty}$	CPU	e_{L^2}	$\mathcal{O}_{L^2}$	e_{L^∞}	$\mathcal{O}_{L^\infty}$	CPU	e_{L^2}	$\mathcal{O}_{L^2}$	e_{L^∞}	$\mathcal{O}_{L^\infty}$	CPU
64^2	3.196E−03	–	6.733E−02	–	7.72	1.625E−03	–	2.864E−02	–	13.05	1.399E−04	–	2.779E−03	–	23.42
128^2	8.814E−04	1.85	1.737E−02	1.95	49.23	3.231E−04	2.33	5.999E−03	2.25	102.67	4.168E−04	−1.57	1.984E−02	−2.83	178.16
256^2	2.223E−04	1.98	4.129E−03	2.07	292.42	9.013E−05	1.84	3.945E−03	0.60	740.22	2.705E−04	0.62	1.154E−02	0.36	1281.26
512^2	9.018E−05	1.30	3.173E−03	0.37	1310.62	4.018E−05	1.16	1.173E−03	1.75	4730.11	1.018E−04	1.41	2.173E−03	2.82	8506.07

Mesh points	MOGV $\mathcal{O}=2$					MOGV $\mathcal{O}=3$					MOGV $\mathcal{O}=4$				
	e_{L^2}	$\mathcal{O}_{L^2}$	e_{L^∞}	$\mathcal{O}_{L^\infty}$	CPU	e_{L^2}	$\mathcal{O}_{L^2}$	e_{L^∞}	$\mathcal{O}_{L^\infty}$	CPU	e_{L^2}	$\mathcal{O}_{L^2}$	e_{L^∞}	$\mathcal{O}_{L^\infty}$	CPU
64^2	4.239E−03	–	9.489E−02	–	7.86	3.245E−03	–	5.866E−02	–	13.23	6.803E−04	–	2.007E−02	–	24.62
128^2	1.256E−03	1.75	2.624E−02	1.85	50.39	6.078E−04	2.41	1.066E−02	2.46	106.48	4.606E−05	3.88	9.210E−04	4.44	191.64
256^2	3.118E−04	2.01	6.225E−03	2.07	302.77	8.522E−05	2.83	1.489E−03	2.84	752.47	2.752E−06	4.06	5.394E−05	4.09	1342.54
512^2	7.018E−05	2.15	1.738E−03	1.84	1321.39	2.018E−05	2.07	2.174E−04	2.77	4810.88	3.018E−07	3.18	3.174E−06	4.08	8615.29

Mesh points	MOGE $\mathcal{O}=2$					MOGE $\mathcal{O}=3$					MOGE $\mathcal{O}=4$				
	e_{L^2}	$\mathcal{O}_{L^2}$	e_{L^∞}	$\mathcal{O}_{L^\infty}$	CPU	e_{L^2}	$\mathcal{O}_{L^2}$	e_{L^∞}	$\mathcal{O}_{L^\infty}$	CPU	e_{L^2}	$\mathcal{O}_{L^2}$	e_{L^∞}	$\mathcal{O}_{L^\infty}$	CPU
64^2	1.752E−03	–	4.048E−02	–	7.91	1.625E−03	–	2.864E−02	–	13.48	1.353E−04	–	2.618E−03	–	25.09
128^2	4.231E−04	2.05	9.738E−03	2.05	51.26	2.685E−04	2.59	4.551E−03	2.65	98.72	7.242E−06	4.22	1.661E−04	3.97	193.24
256^2	1.018E−04	2.05	2.173E−03	2.16	304.01	3.546E−05	2.92	6.052E−04	2.91	758.61	4.109E−07	4.13	8.862E−06	4.22	1352.16
512^2	2.545E−05	2.00	5.425E−04	2.00	1334.59	4.433E−06	2.99	7.565E−05	3.00	4852.66	2.571E−08	4.00	5.540E−07	3.99	8702.93

Mesh points	WENO $\mathcal{O}=2$					WENO $\mathcal{O}=3$					WENO $\mathcal{O}=4$				
	e_{L^2}	$\mathcal{O}_{L^2}$	e_{L^∞}	$\mathcal{O}_{L^\infty}$	CPU	e_{L^2}	$\mathcal{O}_{L^2}$	e_{L^∞}	$\mathcal{O}_{L^\infty}$	CPU	e_{L^2}	$\mathcal{O}_{L^2}$	e_{L^∞}	$\mathcal{O}_{L^\infty}$	CPU
64^2	1.755E−03	–	4.057E−02	–	20.16	1.627E−03	–	2.870E−02	–	38.64	1.355E−04	–	2.624E−03	–	62.61
128^2	4.236E−04	2.05	9.758E−03	2.05	132.24	2.688E−04	2.59	4.560E−03	2.65	217.96	7.250E−06	4.22	1.665E−04	3.97	380.18
256^2	1.019E−04	2.05	2.178E−03	2.16	731.18	3.550E−05	2.92	6.065E−04	2.91	1253.78	4.113E−07	4.13	8.880E−06	4.22	2271.21
512^2	2.548E−05	2.00	5.436E−04	2.00	3521.75	4.438E−06	2.99	7.581E−05	3.00	6980.23	2.573E−08	4.00	5.551E−07	3.99	13234.48

Table 2
L^2 and L^∞ errors and convergence rates, and CPU time ($cores \times time(sec)$) for the 2D vortex evolution problem obtained with various orders of accuracy with the unlimited, MOG, MOGV, MOGE and WENO scheme at the final time of $t = 10$ on triangular meshes.

Mesh points	Unlimited $\mathcal{O}=2$					Unlimited $\mathcal{O}=3$					Unlimited $\mathcal{O}=4$				
	e_{L^2}	$\mathcal{O}_{L^2}$	e_{L^∞}	$\mathcal{O}_{L^\infty}$	CPU	e_{L^2}	$\mathcal{O}_{L^2}$	e_{L^∞}	$\mathcal{O}_{L^\infty}$	CPU	e_{L^2}	$\mathcal{O}_{L^2}$	e_{L^∞}	$\mathcal{O}_{L^\infty}$	CPU
64^2	7.631E−04	–	1.753E−02	–	9.12	6.298E−04	–	9.697E−03	–	17.54	7.858E−05	–	1.384E−03	–	33.81
128^2	1.764E−04	2.11	3.867E−03	2.18	61.14	9.229E−05	2.77	1.372E−03	2.82	130.88	4.568E−06	4.10	8.509E−05	4.02	243.43
256^2	4.278E−05	2.04	8.666E−04	2.16	380.02	1.186E−05	2.96	1.771E−04	2.95	824.54	2.803E−07	4.03	5.134E−06	4.05	1742.97
512^2	1.070E−05	2.00	2.170E−04	2.00	1930.99	1.480E−06	3.00	2.210E−05	3.00	5112.23	1.750E−08	4.00	3.210E−07	4.00	12392.53

Mesh points	MOG $\mathcal{O}=2$					MOG $\mathcal{O}=3$					MOG $\mathcal{O}=4$				
	e_{L^2}	$\mathcal{O}_{L^2}$	e_{L^∞}	$\mathcal{O}_{L^\infty}$	CPU	e_{L^2}	$\mathcal{O}_{L^2}$	e_{L^∞}	$\mathcal{O}_{L^\infty}$	CPU	e_{L^2}	$\mathcal{O}_{L^2}$	e_{L^∞}	$\mathcal{O}_{L^\infty}$	CPU
64^2	8.557E−04	–	1.945E−02	–	9.36	3.415E−03	–	8.936E−02	–	17.93	7.175E−03	–	1.881E−01	–	35.12
128^2	1.996E−04	2.10	4.405E−02	2.14	62.49	1.997E−03	0.77	5.703E−02	0.64	133.29	3.368E−03	1.09	1.047E−01	0.84	247.91
256^2	4.850E−04	2.04	1.015E−03	397.42	292.42	8.464E−04	1.24	4.061E−02	0.49	839.38	1.962E−03	0.78	5.334E−02	0.97	1803.72
512^2	1.278E−05	1.92	2.959E−04	1.78	1976.14	3.278E−04	1.37	7.666E−03	2.41	5163.71	8.278E−04	1.24	8.666E−03	2.62	12584.06

Mesh points	MOGV $\mathcal{O}=2$					MOGV $\mathcal{O}=3$					MOGV $\mathcal{O}=4$				
	e_{L^2}	$\mathcal{O}_{L^2}$	e_{L^∞}	$\mathcal{O}_{L^\infty}$	CPU	e_{L^2}	$\mathcal{O}_{L^2}$	e_{L^∞}	$\mathcal{O}_{L^\infty}$	CPU	e_{L^2}	$\mathcal{O}_{L^2}$	e_{L^∞}	$\mathcal{O}_{L^\infty}$	CPU
64^2	1.188E−03	–	2.888E−02	–	9.68	1.249E−03	–	1.997E−02	–	18.36	1.001E−04	–	3.730E−03	–	35.92
128^2	2.825E−04	2.07	6.585E−02	2.13	64.66	2.055E−04	2.60	3.094E−03	2.69	140.91	7.893E−06	3.66	2.032E−04	4.20	258.67
256^2	6.830E−05	2.05	1.466E−03	2.17	401.36	2.711E−05	2.92	4.179E−04	2.89	851.23	3.608E−07	4.45	6.903E−06	4.88	1834.68
512^2	2.478E−05	1.46	3.666E−03	2.00	1996.80	5.278E−06	2.36	5.666E−05	2.88	5196.84	4.278E−09	3.08	8.659E−07	3.00	12757.92

Mesh points	MOGE $\mathcal{O}=2$					MOGE $\mathcal{O}=3$					MOGE $\mathcal{O}=4$				
	e_{L^2}	$\mathcal{O}_{L^2}$	e_{L^∞}	$\mathcal{O}_{L^\infty}$	CPU	e_{L^2}	$\mathcal{O}_{L^2}$	e_{L^∞}	$\mathcal{O}_{L^\infty}$	CPU	e_{L^2}	$\mathcal{O}_{L^2}$	e_{L^∞}	$\mathcal{O}_{L^\infty}$	CPU
64^2	7.631E−04	–	1.753E−02	–	9.91	6.322E−04	–	9.723E−03	–	18.88	8.568E−05	–	1.670E−03	–	36.28
128^2	1.764E−04	2.11	3.867E−03	2.18	65.29	9.229E−05	2.78	1.372E−03	2.82	143.15	4.623E−06	4.32	9.630E−05	4.12	264.72
256^2	4.278E−05	2.04	8.666E−04	2.16	421.37	1.186E−05	2.96	1.771E−04	2.95	856.17	2.921E−07	3.98	5.907E−06	4.03	1871.55
512^2	1.070E−05	2.00	2.170E−04	2.00	2014.28	1.480E−06	3.00	2.210E−05	3.00	5211.46	1.790E−08	4.03	3.800E−07	3.96	12905.83

Mesh points	WENO $\mathcal{O}=2$					WENO $\mathcal{O}=3$					WENO $\mathcal{O}=4$				
	e_{L^2}	$\mathcal{O}_{L^2}$	e_{L^∞}	$\mathcal{O}_{L^\infty}$	CPU	e_{L^2}	$\mathcal{O}_{L^2}$	e_{L^∞}	$\mathcal{O}_{L^\infty}$	CPU	e_{L^2}	$\mathcal{O}_{L^2}$	e_{L^∞}	$\mathcal{O}_{L^\infty}$	CPU
64^2	7.647E−04	–	1.757E−02	–	32.66	6.311E−04	–	9.718E−03	–	56.32	7.874E−05	–	1.387E−03	–	96.22
128^2	1.768E−04	2.11	3.875E−03	2.18	199.29	9.248E−05	2.77	1.375E−03	2.82	340.45	4.578E−06	4.10	8.527E−05	4.02	632.918
256^2	4.287E−05	2.04	8.684E−04	2.16	1135.58	1.188E−05	2.96	1.774E−04	2.95	1956.25	2.809E−07	4.03	5.145E−06	4.05	3834.53
512^2	1.072E−05	2.00	2.175E−04	2.00	6132.17	1.483E−06	3.00	2.215E−05	3.00	10588.23	1.754E−08	4.00	3.217E−07	4.00	19990.77

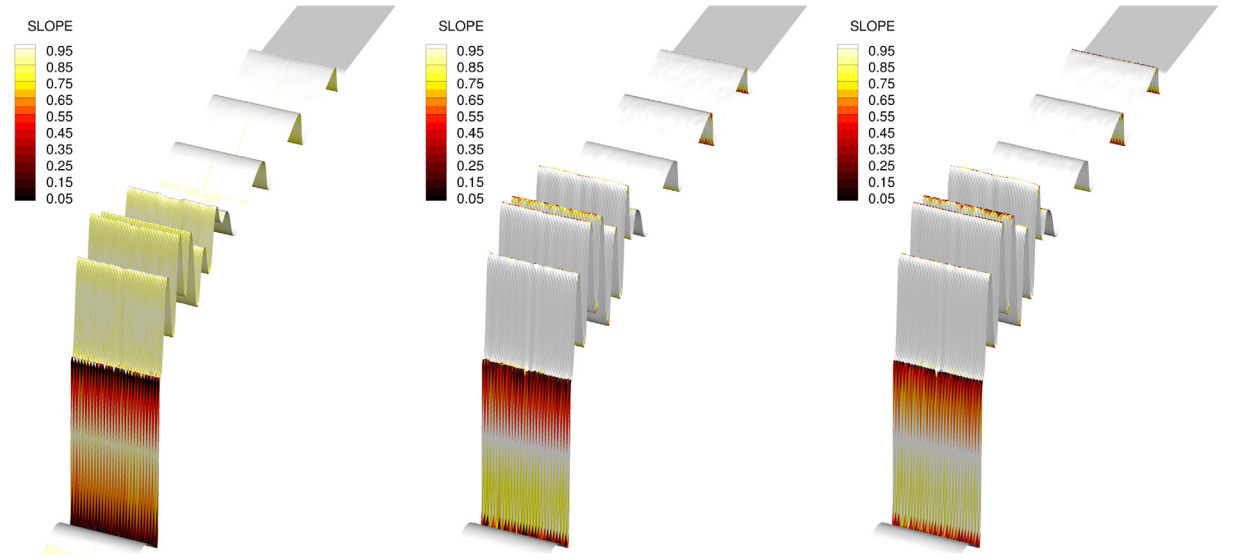


Fig. 10. Density distribution with various 4th-order limiters using the $N = 256$ mesh for the Shu–Osher [71] test problem at $t = 1.8$, coloured by the limiting function ϕ where it can be seen that the MOGV and MOGE schemes do not activate the limiter as often as the MOG scheme. (For interpretation of the colours in this figure, the reader is referred to the web version of this article.)

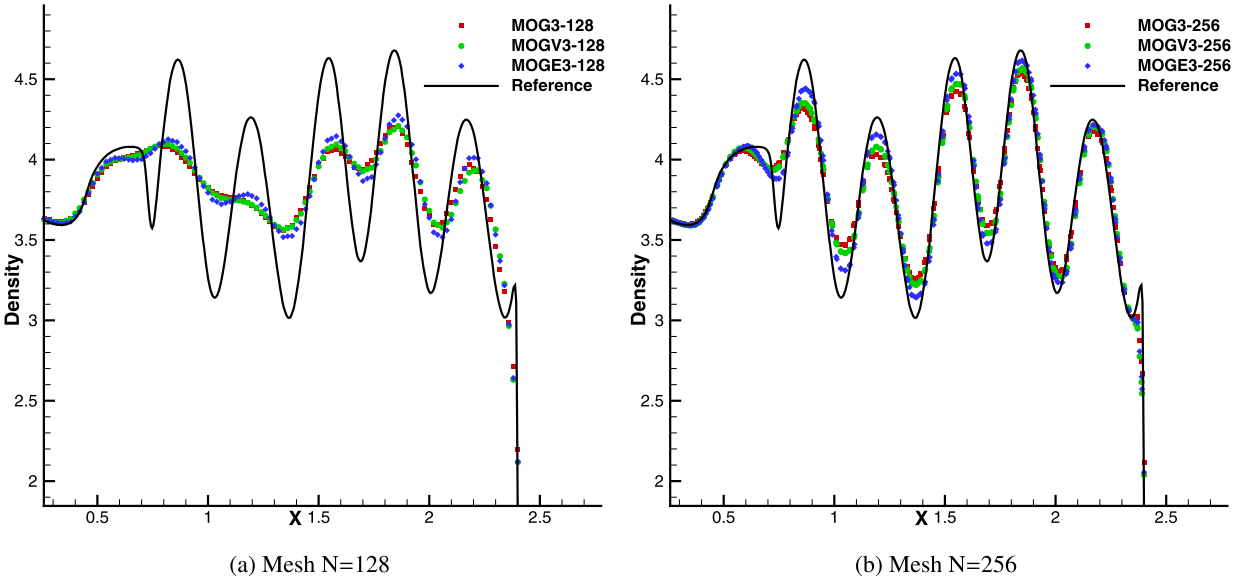
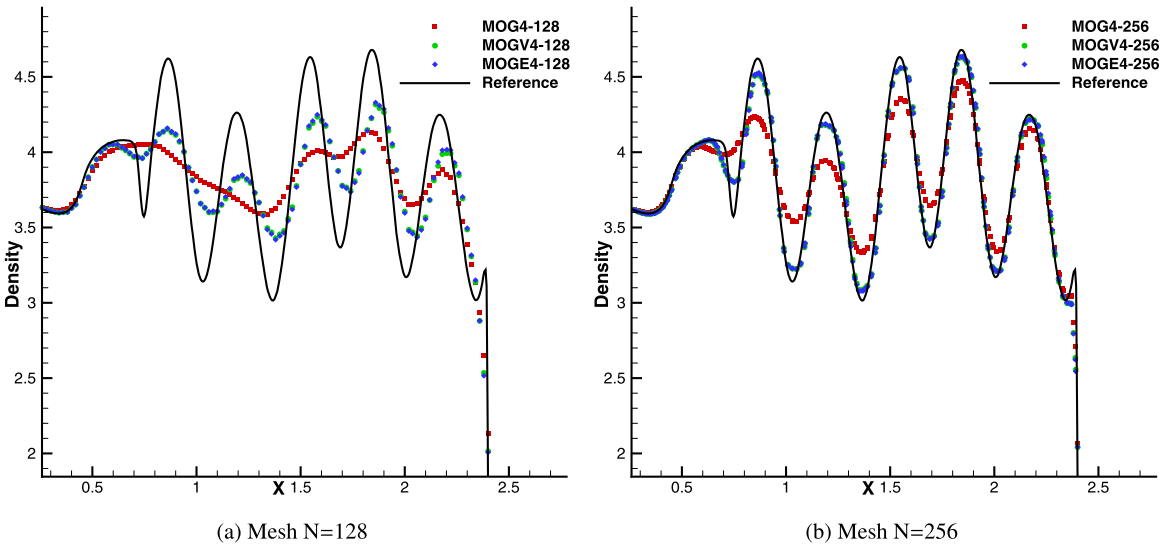


Fig. 11. Density distribution with various 3rd-order limiters using two mesh resolutions for the Shu–Osher [71] shock tube test problem at $t = 1.8$, where the MOGE scheme is in closer agreement with the reference solution. (For interpretation of the references to colour in this figure legend, the reader is referred to the web version of this article.)

Looking closer at the interaction of the entropy wave with the shock wave region as shown at Fig. 11 and Fig. 12 for all the schemes and limiters, it can be noticed that the MOGE and MOGV are consistently more accurate with a sharper profile obtained than the MOG limiter. In conclusion, the MOGE limiter is consistently in closer agreement with the reference solution compared with the MOGV limiter, highlighting that the extended bounds of this limiter do not cause the simulation to diverge or obtain unphysical results.

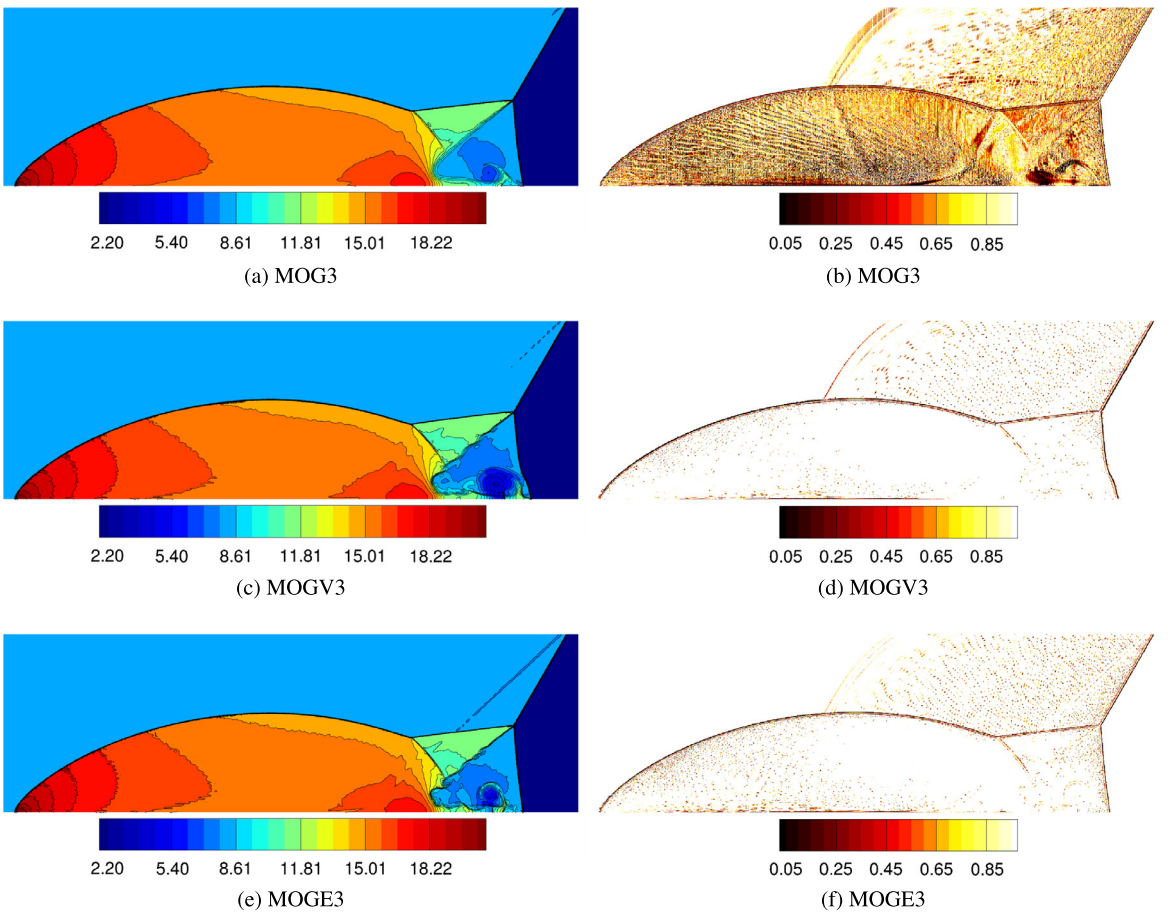
3.3. Double Mach reflection

The double Mach reflection test problem introduced by Woodward and Colella [72] is employed here since it contains various waves and therefore is a well suited problem for assessing the performance of the subject limiters. The initial



(a) Mesh N=128 (b) Mesh N=256

Fig. 12. Density distribution with various 4th-order limiters using two mesh resolutions for the Shu–Osher [71] shock tube test problem at $t = 1.8$, where there is not any improvement for the MOG scheme as opposed to the MOGE and MOGV schemes which are in closer agreement with the reference solution. (For interpretation of the references to colour in this figure legend, the reader is referred to the web version of this article.)



(a) MOG3 (b) MOG3

(c) MOGV3 (d) MOGV3

(e) MOGE3 (f) MOGE3

Fig. 13. Distribution of density and density limiting function ϕ with 3rd-order limiters for the double Mach reflection problem, at $t = 4$. It can be noticed that the limiting function is activated in the correct places for the MOGE, and MOGV schemes, whereas for the MOG scheme it is activated in a large portion of the computational domain. The MOGE and MOGV schemes resolve more flow features than the MOG scheme, and the MOGV scheme produces a more curved Mach stem as seen in the density distribution plots. (For interpretation of the references to colour in this figure legend, the reader is referred to the web version of this article.)

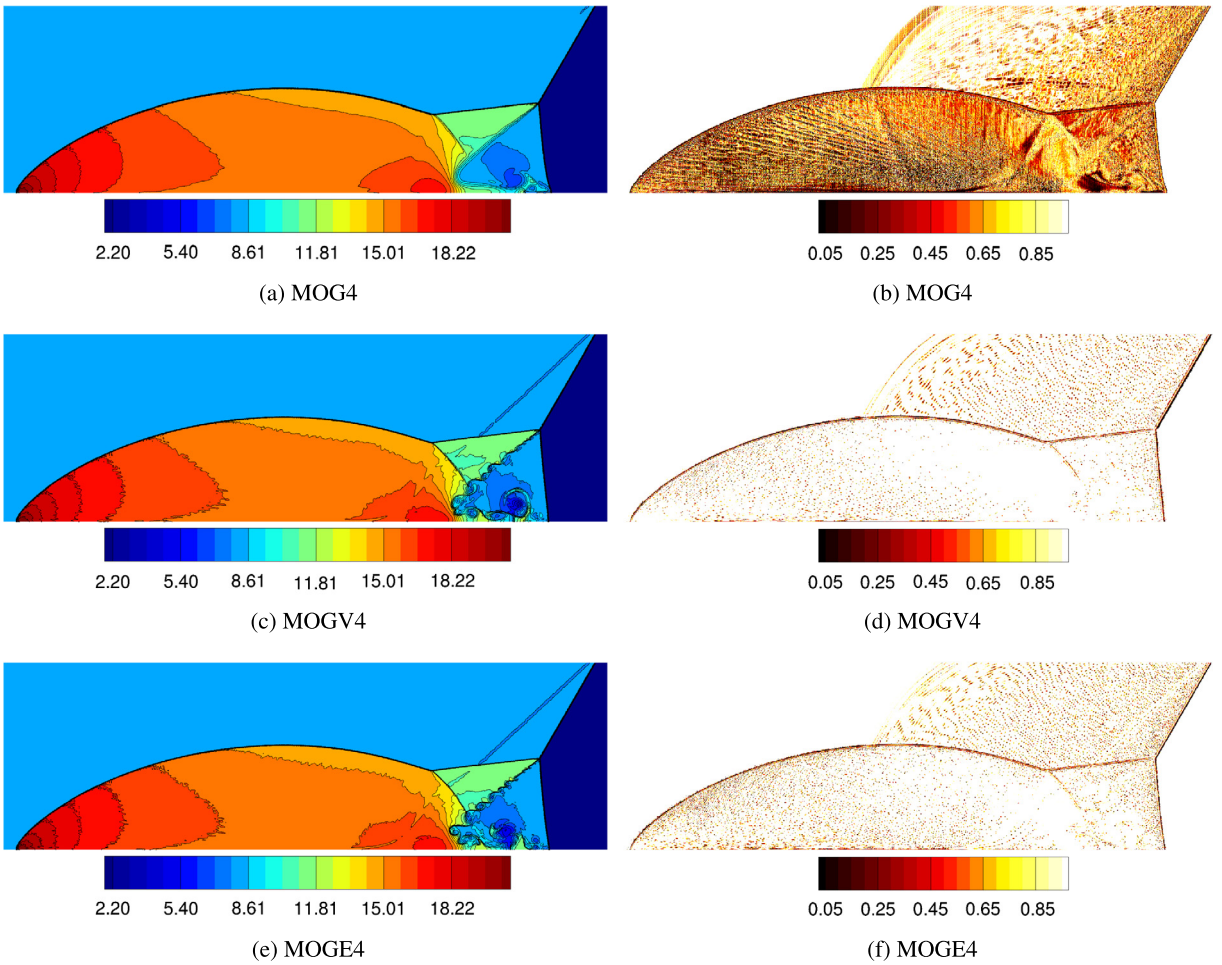


Fig. 14. Distribution of density and density limiting function ϕ with 4th-order limiters for the double Mach reflection problem, at $t = 4$. It can be noticed that the limiting function is activated more frequently for the MOG scheme as opposed to the MOGE and MOGV schemes. The MOGE and MOGV schemes are resolving shear waves and vortex rollup as opposed to the MOG scheme which does not. (For interpretation of the references to colour in this figure legend, the reader is referred to the web version of this article.)

conditions involve a moving shock wave with Mach number $M = 10$ at an inclination of $\alpha = 60°$. The conditions ahead of the shock is at rest with uniform density and pressure $\rho = 1.4$ and $p = 1.0$. Reflecting boundary conditions are used for the bottom of the domain beginning at $x = 1/6$ and post shock conditions before, supersonic inflow boundary conditions on the left side and supersonic outflow boundary conditions on the right side. At the top boundary the exact solution of an isolated moving oblique shock wave with $M = 10$ is prescribed. For additional details the regarding the setup of the problem the reader is referred to Woodward and Colella [72]. The computational domain is given by $[0, 4] \times [0, 1]$ and is discretised by an unstructured mesh of approximately 400,000 triangular cells, that correspond to an equivalent resolution of $h = 1/200$. The 3rd-order and 4th-order numerical schemes are employed with the three limiters. The calculations are performed until time $t = 0.2$, as seen in Fig. 13 and Fig. 14 for the 3rd and 4th order schemes respectively.

All the schemes capture the correct flow pattern with the reflected shock, the two Mach stems and two contact discontinuities. In these figures, the distribution limiting function ϕ for density is also illustrated to highlight which cells required the activation of the limiter. This is quite important for illustrating that the MOG limiter is the one that gets activated at more cells than the other two versions for both the 3rd and the 4th-order schemes. For the 4th-order scheme the activation of the MOGV and MOGE limiters is more pronounced than in the 3rd-order scheme, which is expected since either sharp gradient, or pressure waves created by the rolling of the shear waves, or the grid-topology itself can cause the limiter to be activated since the reconstructed solution violates the bounds. In Fig. 15 the density distribution at the vortex interaction zone is zoomed in for appreciating the differences between the schemes. It is quite clear that the 4th-order schemes resolve more vortices than the 3rd-order schemes, as expected but this is true only for the MOGV and MOGE limiters, since the MOG limiter fails to capture any vortex rollup due to the excessive activation of the limiter itself. Nevertheless, the differences between the MOGE and MOGV limiters for this test-problem are minimal for the 4th-order of accuracy, but significant for the 3rd-order since the MOGE scheme resolves more shear waves compared to the MOGV scheme. Additionally

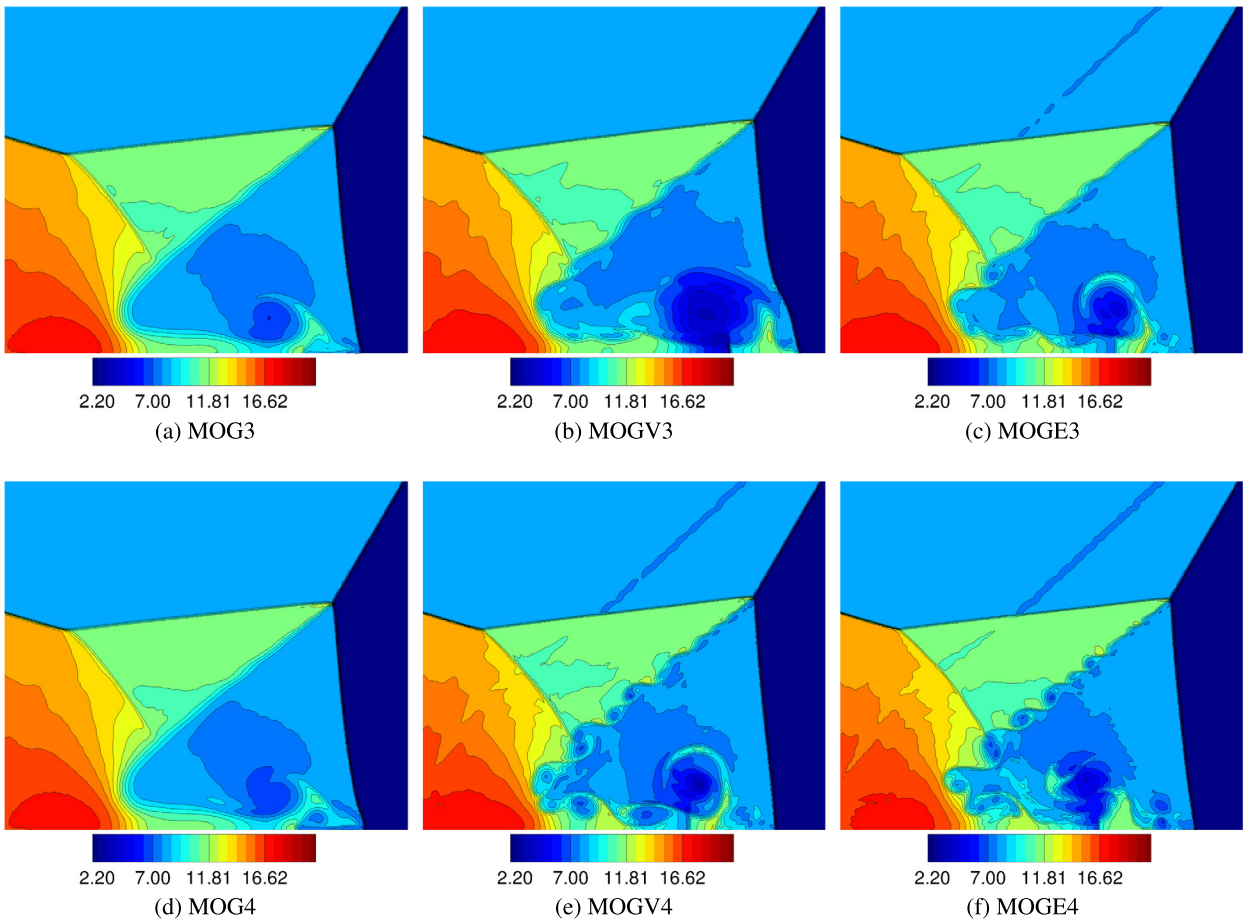


Fig. 15. Density distribution with various limiters for the double Mach reflection problem at $t = 4$. Zoomed on the wave interaction zone where it can be noticed that the differences between the MOGE and MOGV schemes are significant for the 3rd-order with the MOGE scheme resolving more flow features and the MOGV scheme producing a curved Mach stem. For the 4th-order the MOGE scheme produces marginally more pronounced shear waves compared to the MOGV scheme, and the MOG scheme fails to resolve the flow features that the other two schemes resolve. (For interpretation of the references to colour in this figure legend, the reader is referred to the web version of this article.)

for the MOGV3 scheme a more curved Mach stem is noticed, resembling a Triple-Mach White-Reflection TM-WR as documented by other computational and experimental studies [73,74]. It can be attributed to the current setup of the problem where a rectangular computational domain is used and the shock wave is inclined with respect to the grid, and due to the nature of the unstructured mesh employed perturbations in the initial profile of the shock wave can result in this flow feature.

3.4. Mach 3 forward facing step

The Mach 3 forward facing step test problem introduced by Woodward and Colella [72] is employed here since it involves a flow with complex structures of interacting shocks. The size of the domain is 3 units length with the step placed at 0.6 length units from the left side of the domain, and is having a height of 0.2 units. An ideal gas is considered with constant density $\rho = 1.4$, velocity $(u, v) = (3, 0)$ and pressure $p = 1.0$. A supersonic inflow condition is applied on the left, a supersonic outflow condition on the right and reflective boundary conditions on the upper and lower sides. The computational domain is discretised by an unstructured mesh of approximately $180,000$ triangular cells, that correspond to an equivalent resolution of $h = 1/200$. For avoiding the singularity point at the corner of the step the corner was rounded off as suggested in [75] with a curvature of radius 0.003. The 3rd-order and 4th-order numerical schemes are employed with the three limiters. The calculations are performed until time $t = 4.0$, as seen in Fig. 16 and Fig. 17 for the 3rd and 4th order schemes respectively.

All the schemes capture the correct flow pattern with the contact discontinuity resulting from the three-shock interaction. It can be noticed that the limiting action for the MOGE and MOGV limiters occurs only in the places where it is needed which is across the waves with sharp gradients. For the MOG limiter as in the previous test problem the sensitivity of the limiter activates it for an overwhelming number of cells in the domain. The resulting difference in the results

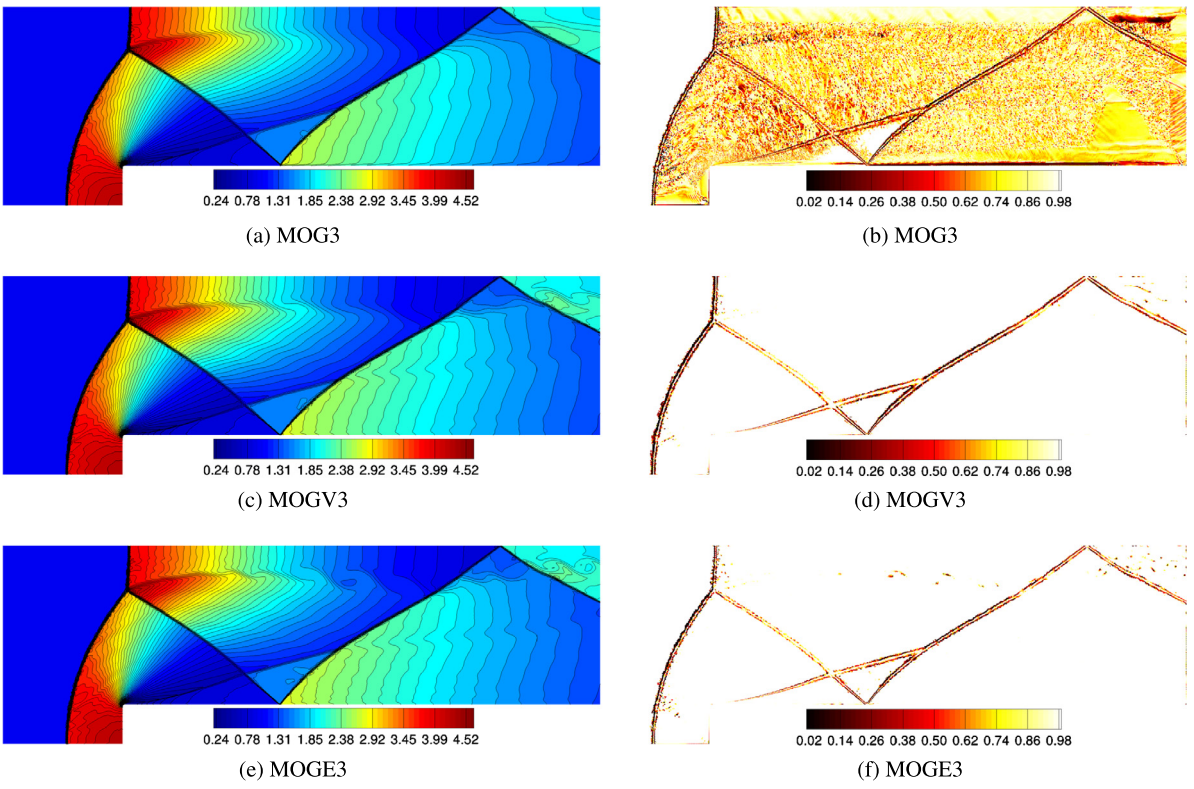


Fig. 16. Distribution of density and density limiting function ϕ with 3rd-order limiters for the Mach 3 forward facing step problem, at $t = 4$. It can be noticed that the limiting function is activated more frequently for the largest portion of the domain for the MOG scheme as opposed to the MOGE and MOGV schemes. The MOGE resolves more instabilities than the MOGV scheme across the contact discontinuity. (For interpretation of the colours in this figure, the reader is referred to the web version of this article.)

is more pronounced in Fig. 18 where the region at which the Kelvin–Helmholtz instabilities develop along the contact discontinuity is zoomed in. It is obvious that the MOGE limiter has the best resolution in terms of the Kelvin–Helmholtz instabilities compared to the MOGV limiter for both the 3rd- and 4th-order schemes. However it only the MOGE and MOGV limiters that can capture the Kelvin–Helmholtz instabilities highlighting the more restrictive performance of the MOG limiter.

3.5. 2D Riemann problem

The performance of the limiters is assessed in the widely used 2D Riemann problem for Euler equations introduced by Schulz et al. [76]. The computational domain is $[-0.5, 0.5] \times [-0.5, 0.5]$ and the initial condition is represented by the four different states assigned to each of the quadrants of the domain as shown in Fig. 19, with the adiabatic gas constant $\gamma = 1.4$. The computational domain has been discretised by a hybrid unstructured mesh of approximately $831,000$ elements consisting of quadrilateral and triangular elements. The lower left quadrant has been refined and has the equivalent resolution of approximately $h = 1/1818$. The simulation has been performed until $t = 0.5$. It was considered essential to compare the limiters employed to a WENO scheme of the same order of accuracy that has a computational cost of approximately 1.7 more than the MOGE and MOGV schemes in their current implementation in the employed CFD code UCNS3D [4,5,8,57–60]. For further details regarding the WENO scheme employed the reader is referred to [4,5].

From the obtained results in Fig. 20 it can be noticed that due to the high-order of accuracy of the schemes and the fine grid resolution, several small-scale flow features appear in the solution. The roll-up of the Kelvin–Helmholtz instability is very sharply captured by the all the schemes, the main difference lies in the number of roll-ups and small-scale features that each scheme resolves. WENO scheme provides the largest number of small-scale structures as it was expected, however it is approximately 185% more expensive than the MOGE scheme for the present test problem. MOGE has more pronounced Kelvin–Helmholtz instabilities at the Mach stem and the roll-up is more prominent as opposed to MOGV and MOG limiters. Equally, to the previous tests the MOG limiter exhibits the largest numerical dissipation due to activation of the limiting process, hence the number of flow-structures is reduced compared to the other limiters.

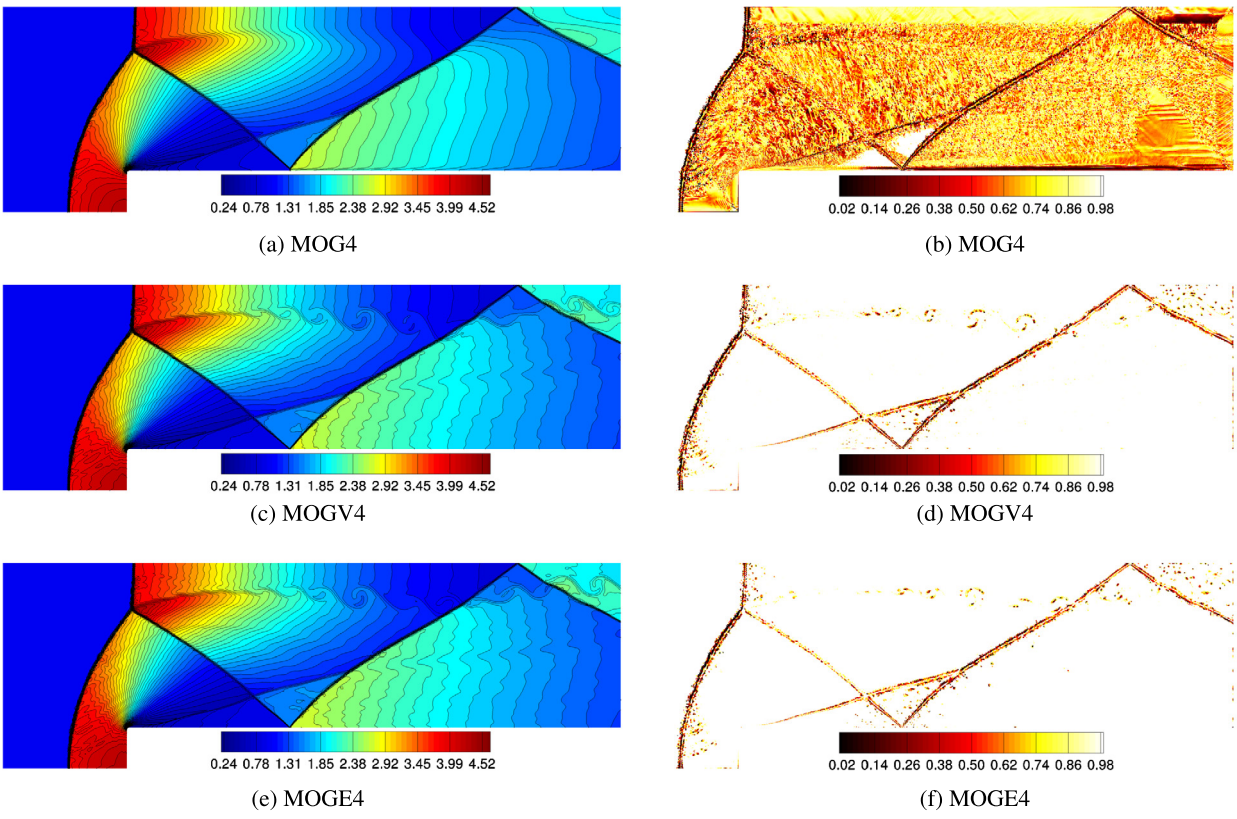


Fig. 17. Distribution of density and density limiting function ϕ with 4th-order limiters for the Mach 3 forward facing step problem, at $t = 4$. It can be noticed that the limiting function is activated at the expected places only for the MOGE and MOGV schemes. The MOGE and MOGV schemes resolve more flow features and the differences between them are minimal. (For interpretation of the colours in this figure, the reader is referred to the web version of this article.)

3.6. Shock-wave in cylindrical cavity

The final test problem involves the interaction of a shock wave with a cylindrical cavity, a test-problem defined experimentally by Skews and Kleine [77] and investigated computationally by Diot et al. [2]. A cylindrical cavity is considered as seen in Fig. 21, with a shock wave of Mach number $M = 1.33$. The initial profile consists of a post-shock region $(\rho, u, v, p) = (1.7522, 166.3435, 0, 180219.75)$ on the left side of the domain, and the pre-shock region on the right $(\rho, u, v, p) = (1.1175, 0, 0, 95000)$. It was chosen to refine the pre-shock region as shown in Fig. 21, since this is the region of interest for the current test problem. A supersonic inflow is applied on the left side with the post-shock conditions, a supersonic outflow on the right-side outlet, and reflective boundary conditions in the rest of the domain. Similarly, to Diot et al. [2] the simulation is performed only for the lower-half of the domain using the symmetry assumption. The mesh consists of approximately 300,000 cells including triangles and quadrilateral elements. The simulation is run until $t \approx 0.00062$ using the 4th-order limiters, and for illustration purposes and comparison with the experimental results the images are rendered as the full domain.

From the obtained results as seen in Fig. 22 it can be noticed that the obtained results with all the schemes are in agreement with the experimental results of Skews and Kleine [77] at the equivalent times of Fig. 7(a), Fig. 8(d) and Fig. 9(c) of [77]. It is evident that the results obtained with the MOGE limiter the obtained flow features are crispier compared to the other two. From the zoomed in solutions at late times as shown in Fig. 23 and Fig. 24, the difference between the limiters is more pronounced where the MOGE limiter results in an increased number of vortices and instabilities compared to the other two, which is in closer agreement with the experimental results.

4. Conclusions

This paper follows in the footsteps of the high-order limiter introduced by Michalak and Ollivier-Gooch [56], and a number of modifications are presented. The key characteristics of the modified limiters are the stencil elements that are used to establish the bounds of the reconstructed solution. Using the direct side neighbours for establishing the bounds results in sub-optimal order of accuracy, since the limiter can be mistakenly activated due to the grid-topology and grid-quality. In contrast, the modified versions of the limiters use either all the neighbours of the vertices or all the elements of the

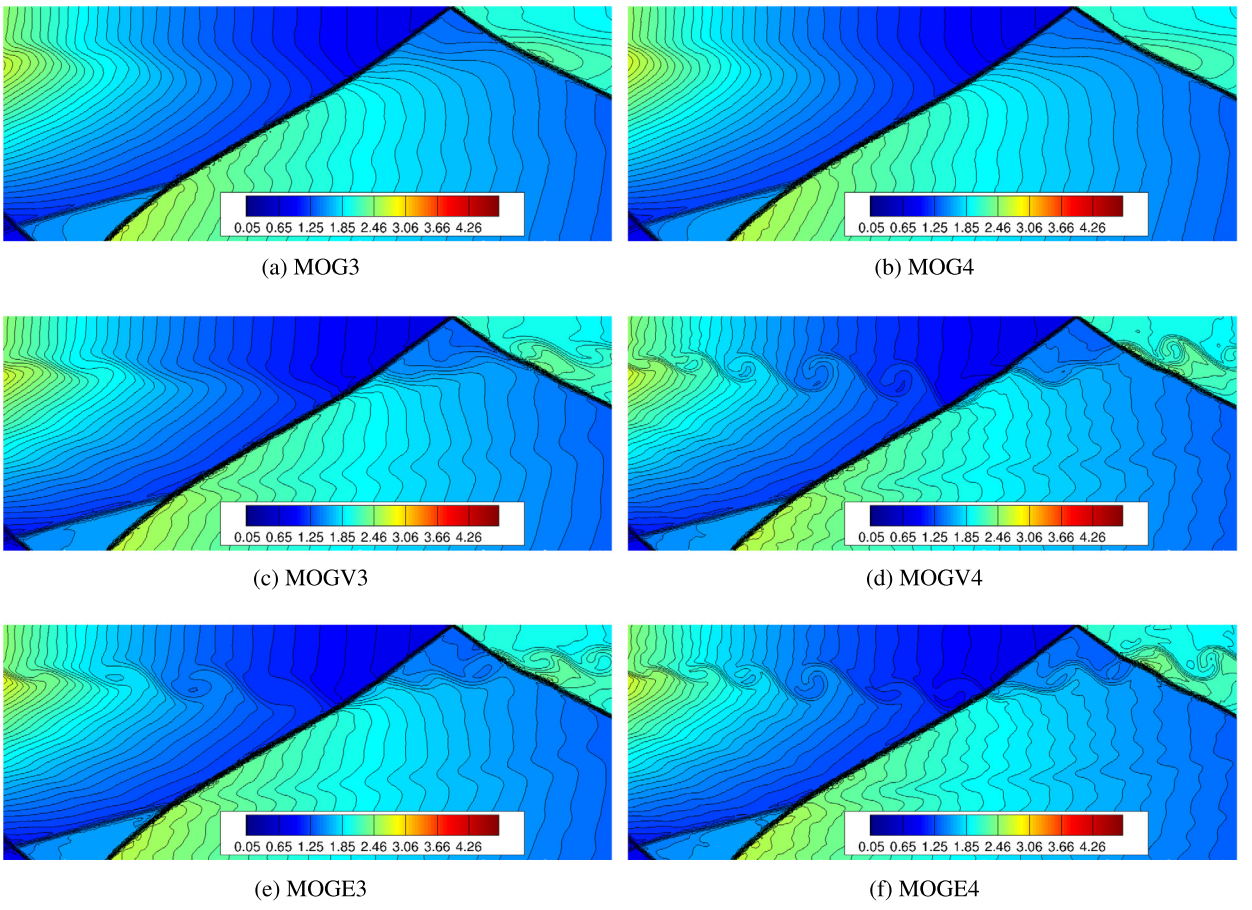


Fig. 18. Density distribution with various limiters for the Mach 3 forward facing step problem, at $t = 4$. Zoomed on the instabilities. The MOGE scheme is the only one that can capture the formation of some Kelvin–Helmholtz instabilities along the contact discontinuity even with the 3rd-order of accuracy, whereas the MOG scheme fails to capture any of them. (For interpretation of the colours in this figure, the reader is referred to the web version of this article.)

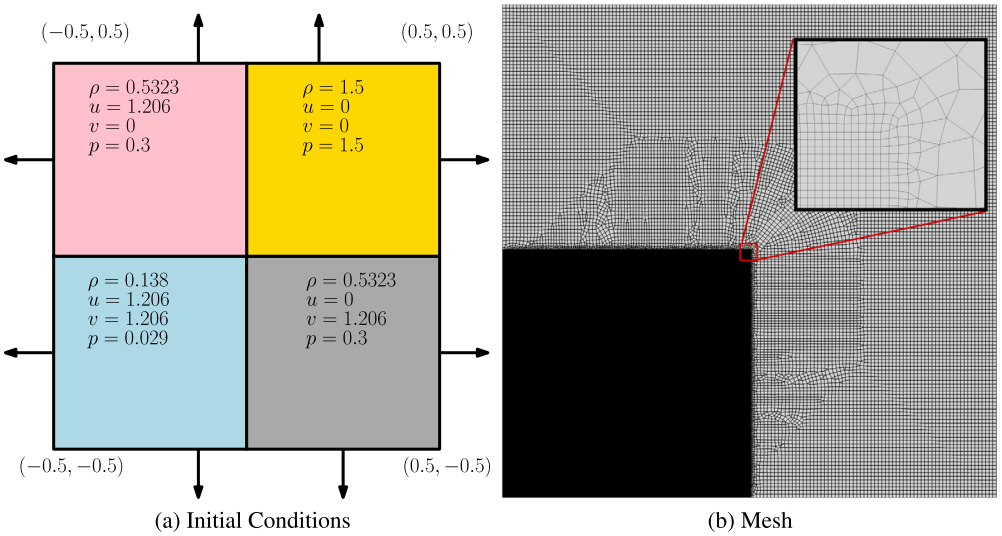
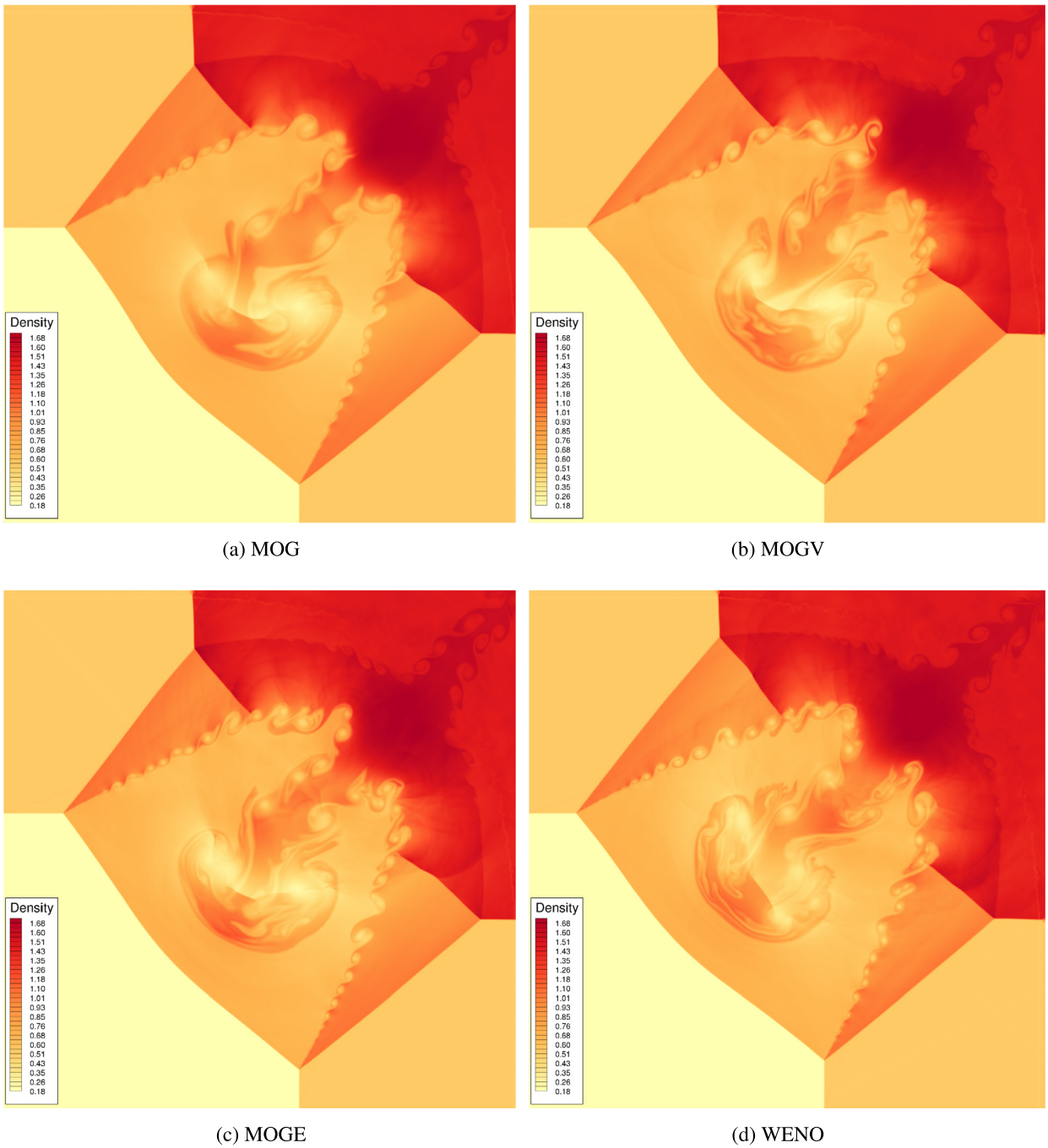


Fig. 19. Initial conditions and mesh for the multidimensional Riemann problem.



(a) MOG (b) MOGV

(c) MOGE (d) WENO

Fig. 20. Density distribution with various 4th-order numerical schemes for the multidimensional Riemann problem at $t_{final} = 1.0$. Only the lower left portion of the computational domain is shown. It can be noticed that the MOGE scheme is in closer agreement with the WENO scheme with a more prominent roll-up and largest number of small-scale structures in the shear layer compared to the MOG and MOGV schemes. (For interpretation of the colours in this figure, the reader is referred to the web version of this article.)

stencil for the MOGV and MOGE limiters respectively. By applying these limiters to several stringent applications for Euler equations, the benefits of the modified limiters are presented, showing that they work well for smooth and discontinuous flow problems. Finally, the best performance is achieved with the MOGE limiter, which has the bounds defined by all the elements in the stencil, resulting in a limiter with wider range of bounds and therefore better accuracy. Considering that the computational cost of the MOGE limiter is significant lower than a WENO type scheme, it could be used as a cost-effective option for a variety of flow problems. Future work involves expanding the scheme to 3D applications, where the computational savings with respect to WENO schemes are considered to be more significant than in 2D.

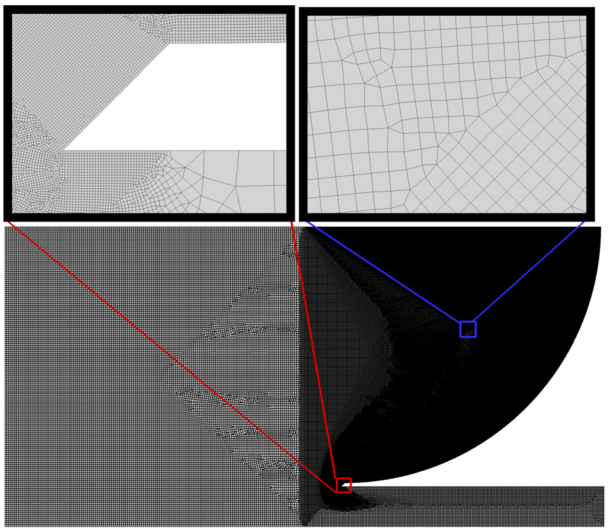


Fig. 21. Overview of the hybrid unstructured mesh used for the cylindrical cavity test problem.

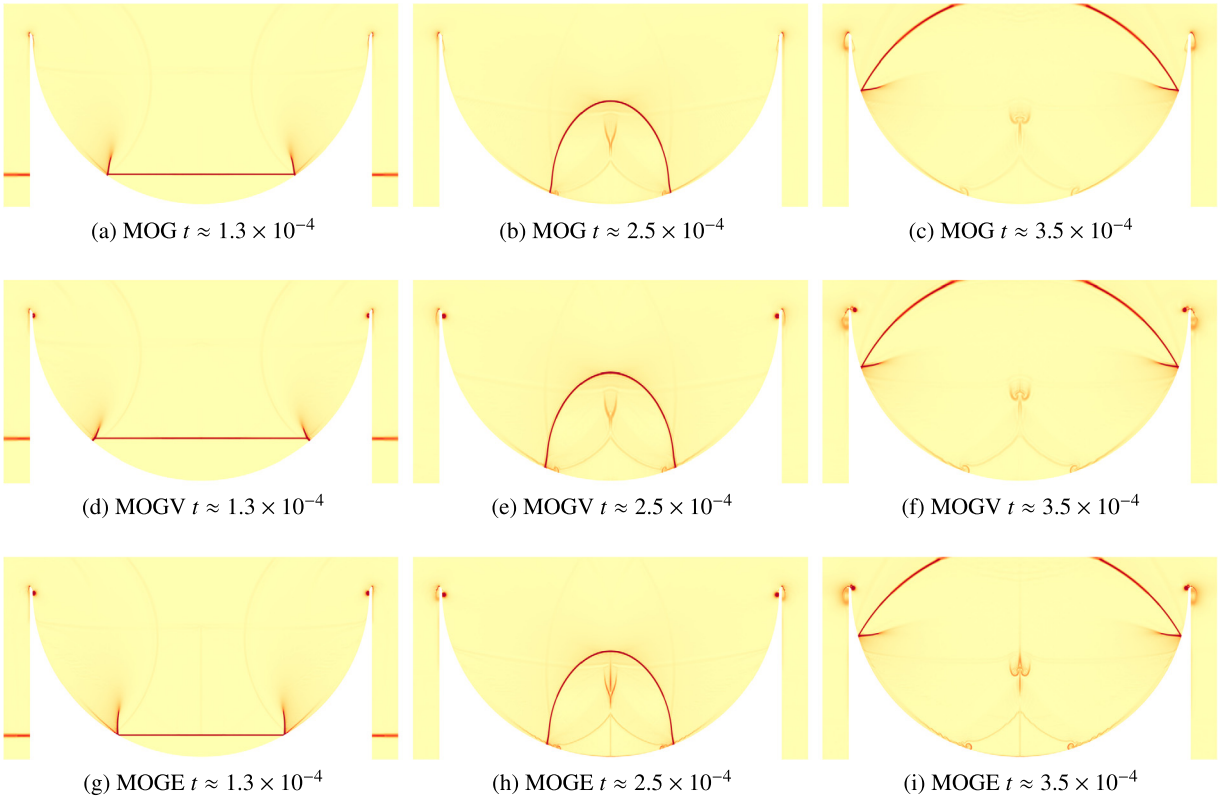
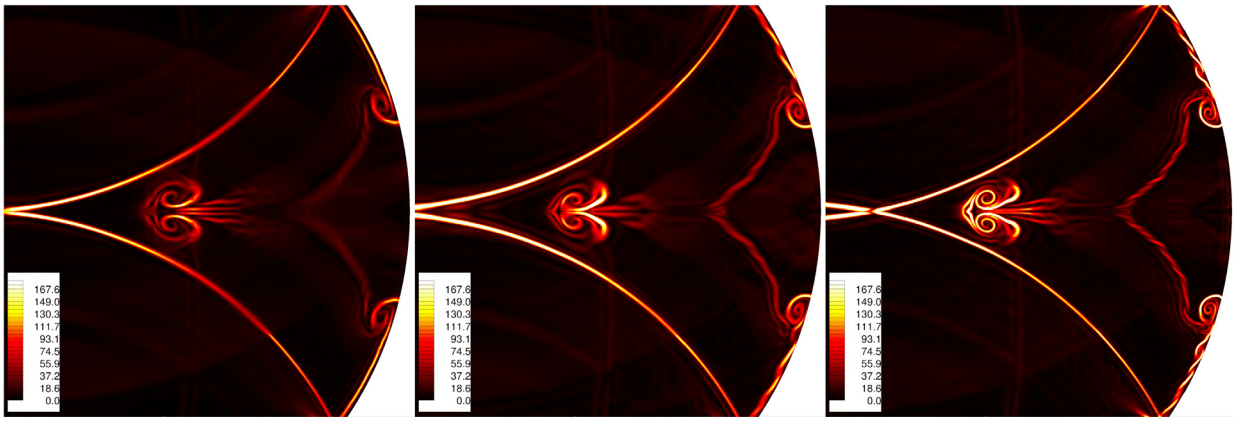


Fig. 22. Distribution of the density gradient magnitude with 4th-order limiters for the shock on cylindrical cavity test problem at different times. The MOGE scheme provides the sharpest resolution of all the flow features, compared to the other two schemes.

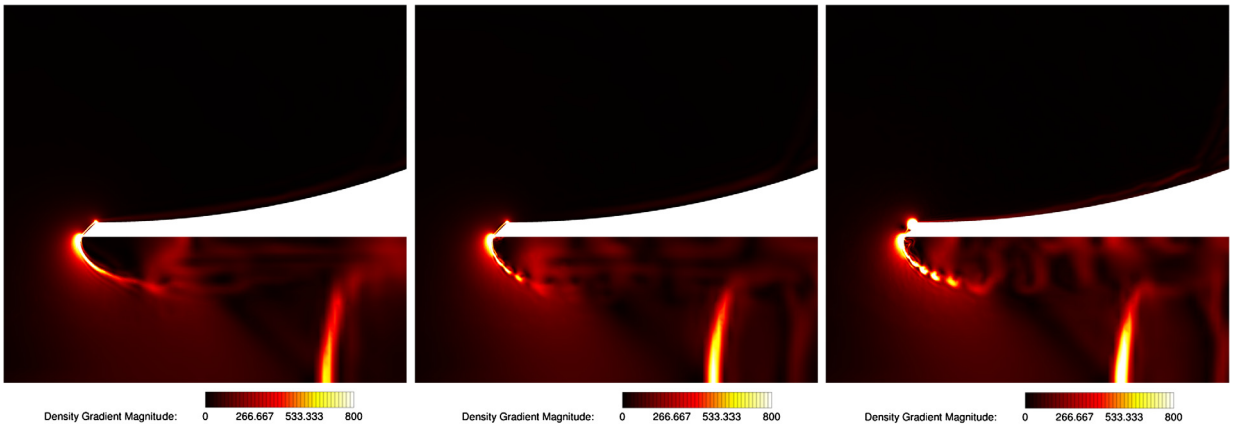
Acknowledgements

The author acknowledges the computing time on the UK national high-performance computing service ARCHER that was provided through the UK Turbulence Consortium in the framework of the EPSRC grant EP/L000261/1 and the computing time at HAZELHEN at the High-Performance Computing Center Stuttgart (HLRS), Germany and SuperMUC at the Leibniz Supercomputing Centre (LRZ) in Garching, Germany in the framework of the PRACE project funded in part by the EU Horizon



(a) MOG (b) MOGV (c) MOGE

Fig. 23. Distribution of the density gradient magnitude with 4th-order limiters for the shock on cylindrical cavity test problem at $t \approx 6.2 \times 10^{-4}$. It can be noticed that the MOGE scheme results are characterised by an increased number of vortices and instabilities compared to the other schemes. (For interpretation of the colours in this figure, the reader is referred to the web version of this article.)



(a) MOG (b) MOGV (c) MOGE

Fig. 24. Distribution of the density gradient magnitude with 4th-order limiters for the shock on cylindrical cavity test problem at $t \approx 6.2 \times 10^{-4}$, zoomed region of the cavity entry. It can be seen that the MOGE scheme resolves more vortical structures than the MOGV scheme. (For interpretation of the colours in this figure, the reader is referred to the web version of this article.)

2020 research and innovation programme (2014–2020) under grant agreement 653838. The author also acknowledges the constructive comments and suggestions provided by the anonymous reviewers that improved the paper.

References

[1] P. Bakhvalov, T. Kozubskaya, EBR-WENO scheme for solving gas dynamics problems with discontinuities on unstructured meshes, Comput. Fluids 157 (2017) 312–324.
[2] S. Diot, S. Clain, R. Loubére, Improved detection criteria for the multi-dimensional optimal order detection (MOOD) on unstructured meshes with very high-order polynomials, Comput. Fluids 64 (2012) 43–63, https://doi.org/10.1016/j.compfluid.2012.05.004.
[3] L. Cueto-Felgueroso, I. Colominas, J. Fe, F. Navarrina, M. Casteleiro, High-order finite volume schemes on unstructured grids using moving least-squares reconstruction: application to shallow water dynamics, Int. J. Numer. Methods Eng. 65 (3) (2006) 295–331, https://doi.org/10.1002/nme.1442.
[4] P. Tsoutsanis, V. Titarev, D. Drikakis, WENO schemes on arbitrary mixed-element unstructured meshes in three space dimensions, J. Comput. Phys. 230 (4) (2011) 1585–1601.
[5] P. Tsoutsanis, A. Antoniadis, D. Drikakis, WENO schemes on arbitrary unstructured meshes for laminar, transitional and turbulent flows, J. Comput. Phys. 256 (2014) 254–276.
[6] C. Ollivier-Gooch, A. Nejat, K. Michalak, Obtaining and verifying high-order unstructured finite volume solutions to the Euler equations, AIAA J. 47 (9) (2009) 2105–2120, https://doi.org/10.2514/1.40585.
[7] A. Nejat, C. Ollivier-Gooch, A high-order accurate unstructured finite volume Newton–Krylov algorithm for inviscid compressible flows, J. Comput. Phys. 227 (4) (2008) 2582–2609, https://doi.org/10.1016/j.jcp.2007.11.011.
[8] P. Tsoutsanis, I. Kokkinakis, L. Konozsy, D. Drikakis, R. Williams, D. Youngs, Comparison of structured- and unstructured-grid, compressible and incompressible methods using the vortex pairing problem, Comput. Methods Appl. Mech. Eng. 293 (2015) 207–231, https://doi.org/10.1016/j.cma.2015.04.010.
[9] V. Titarev, P. Tsoutsanis, D. Drikakis, WENO schemes for mixed-element unstructured meshes, Comput. Phys. Commun. 8 (3) (2010) 585–609.
[10] G. Lei, W. Li, Y. Ren, High-order unstructured-grid WENO FVM for compressible flow computation, Jisuan Wuli/Chin. J. Comput. Phys. 28 (5) (2011) 633–640.

[11] W. Li, Y.-X. Ren, High-order k-exact WENO finite volume schemes for solving gas dynamic Euler equations on unstructured grids, Int. J. Numer. Methods Fluids 70 (6) (2012) 742–763.
[12] G. Hu, R. Li, T. Tang, A robust WENO type finite volume solver for steady Euler equations on unstructured grids, Commun. Comput. Phys. 9 (3) (2011) 627–648.
[13] H.-S. Zheng, N. Zhao, J. Zhu, High order finite volume weighted essentially non-oscillatory schemes on two dimensional unstructured meshes, Kongqi Donglixue Xuebao/Acta Aerodyn. Sin. 28 (4) (2010) 446–451.
[14] X. Nogueira, L. Cueto-Felgueroso, I. Colominas, F. Navarrina, M. Casteleiro, A new shock-capturing technique based on moving least squares for higher-order numerical schemes on unstructured grids, Comput. Methods Appl. Mech. Eng. 199 (37–40) (2010) 2544–2558.
[15] M. Dumbser, D. Balsara, E. Toro, C.-D. Munz, A unified framework for the construction of one-step finite volume and discontinuous Galerkin schemes on unstructured meshes, J. Comput. Phys. 227 (18) (2008) 8209–8253.
[16] M. Dumbser, M. Kaser, V. Titarev, E. Toro, Quadrature-free non-oscillatory finite volume schemes on unstructured meshes for nonlinear hyperbolic systems, J. Comput. Phys. 226 (1) (2007) 204–243.
[17] M. Dumbser, M. Kaser, Arbitrary high order non-oscillatory finite volume schemes on unstructured meshes for linear hyperbolic systems, J. Comput. Phys. 221 (2) (2007) 693–723.
[18] M. Ciardi, P. Sagaut, M. Klein, W. Dawes, A dynamic finite volume scheme for large-eddy simulation on unstructured grids, J. Comput. Phys. 210 (2) (2005) 632–655.
[19] R. Abgrall, On essentially non-oscillatory schemes on unstructured meshes: analysis and implementation, J. Comput. Phys. 114 (1) (1994) 45–58.
[20] O. Friedrich, Weighted essentially non-oscillatory schemes for the interpolation of mean values on unstructured grids, J. Comput. Phys. 144 (1) (1998) 194–212.
[21] D. De Grazia, G. Mengaldo, D. Moxey, P. Vincent, S. Sherwin, Connections between the discontinuous Galerkin method and high-order flux reconstruction schemes, Int. J. Numer. Methods Fluids 75 (12) (2014) 860–877, https://doi.org/10.1002/fld.3915.
[22] D. Kuzmin, A vertex-based hierarchical slope limiter for p-adaptive discontinuous Galerkin methods, J. Comput. Appl. Math. 233 (12) (2010) 3077–3085, https://doi.org/10.1016/j.cam.2009.05.028.
[23] H. Hoteit, P. Ackerer, R. Mose, J. Erhel, B. Philippe, New two-dimensional slope limiters for discontinuous Galerkin methods on arbitrary meshes, Int. J. Numer. Methods Eng. 61 (14) (2004) 2566–2593, https://doi.org/10.1002/nme.1172.
[24] J. Zhu, J. Qiu, Hermite WENO schemes and their application as limiters for Runge–Kutta discontinuous Galerkin method, iii: unstructured meshes, J. Sci. Comput. 39 (2) (2009) 293–321.
[25] Z. Xu, Y. Liu, C.-W. Shu, Hierarchical reconstruction for discontinuous Galerkin methods on unstructured grids with a WENO-type linear reconstruction and partial neighbouring cells, J. Comput. Phys. 228 (6) (2009) 2194–2212.
[26] J. Zhu, J. Qiu, C.-W. Shu, M. Dumbser, Runge–Kutta discontinuous Galerkin method using WENO limiters ii: unstructured meshes, J. Comput. Phys. 227 (9) (2008) 4330–4353.
[27] H. Luo, J. Baum, R. Lohner, A Hermite WENO-based limiter for discontinuous Galerkin method on unstructured grids, J. Comput. Phys. 225 (1) (2007) 686–713.
[28] F. Giraldo, High-order triangle-based discontinuous Galerkin methods for hyperbolic equations on a rotating sphere, J. Comput. Phys. 214 (2) (2006) 447–465.
[29] X. Zhang, Y. Xia, C.-W. Shu, Maximum-principle-satisfying and positivity-preserving high order discontinuous Galerkin schemes for conservation laws on triangular meshes, J. Sci. Comput. (2011) 1–34.
[30] Z. Wang, Spectral (finite) volume method for conservation laws on unstructured grids: basic formulation, J. Comput. Phys. 178 (1) (2002) 210–251.
[31] Z. Wang, L. Zhang, Y. Liu, Spectral (finite) volume method for conservation laws on unstructured grids, iv: extension to two-dimensional systems, J. Comput. Phys. 194 (2) (2004) 716–741.
[32] Z. Wang, Y. Liu, Spectral (finite) volume method for conservation laws on unstructured grids, ii: extension to two-dimensional scalar equation, J. Comput. Phys. 179 (2) (2002) 665–697.
[33] Y. Liu, M. Vinokur, Z. Wang, Spectral difference method for unstructured grids, i: basic formulation, J. Comput. Phys. 216 (2) (2006) 780–801.
[34] Y. Sun, Z. Wang, Y. Liu, Spectral (finite) volume method for conservation laws on unstructured grids, vi: extension to viscous flow, J. Comput. Phys. 215 (1) (2006) 41–58.
[35] G. Mengaldo, D. De Grazia, D. Moxey, P. Vincent, S. Sherwin, Dealiasing techniques for high-order spectral element methods on regular and irregular grids, J. Comput. Phys. 299 (2015) 56–81, https://doi.org/10.1016/j.jcp.2015.06.032.
[36] C. Breviglieri, A. Maximiliano, E. Basso, J. Azevedo, Improved high-order spectral finite volume method implementation for aerodynamic flows, in: 27th AIAA Applied Aerodynamics Conference, 79128, 2009.
[37] Z. Xu, Y. Liu, C.-W. Shu, Hierarchical reconstruction for spectral volume method on unstructured grids, J. Comput. Phys. 228 (16) (2009) 5787–5802.
[38] P. Vincent, A. Farrington, F. Witherden, A. Jameson, An extended range of stable-symmetric-conservative flux reconstruction correction functions, Comput. Methods Appl. Mech. Eng. 296 (2015) 248–272, https://doi.org/10.1016/j.cma.2015.07.023.
[39] D. Williams, P. Castonguay, P. Vincent, A. Jameson, Energy stable flux reconstruction schemes for advection–diffusion problems on triangles, J. Comput. Phys. 250 (2013) 53–76, https://doi.org/10.1016/j.jcp.2013.05.007.
[40] P. Castonguay, P. Vincent, A. Jameson, A new class of high-order energy stable flux reconstruction schemes for triangular elements, J. Sci. Comput. 51 (1) (2012) 224–256, https://doi.org/10.1007/s10915-011-9505-3.
[41] J. Bull, A. Jameson, High-order flux reconstruction schemes for LES on tetrahedral meshes, Notes Numer. Fluid Mech. Multidiscipl. Des. 130 (2015) 69–79, https://doi.org/10.1007/978-3-319-15141-0_5.
[42] B. van Leer, Towards the ultimate conservative difference scheme, v: a second-order sequel to Godunov's method, J. Comput. Phys. 32 (1) (1979) 101–136.
[43] B. Van Leer, Towards the ultimate conservative difference scheme, iv: a new approach to numerical convection, J. Comput. Phys. 23 (3) (1977) 276–299.
[44] B. van Leer, Towards the ultimate conservative difference scheme, ii: monotonicity and conservation combined in a second-order scheme, J. Comput. Phys. 14 (4) (1974) 361–370.
[45] A. Harten, B. Engquist, S. Osher, S. Chakravarthy, Uniformly high order accurate essentially non-oscillatory schemes, iii, J. Comput. Phys. 71 (2) (1987) 231–303.
[46] G.S. Jiang, C.W. Shu, Efficient implementation of weighted ENO schemes, J. Comput. Phys. 126 (1) (1996) 202–228.
[47] C.-W. Shu, TVB uniformly high-order schemes for conservation laws, Math. Comput. 49 (179) (1987) 105–121.
[48] S. Clain, S. Diot, R. Loubère, A high-order finite volume method for systems of conservation laws-multi-dimensional optimal order detection (MOOD), J. Comput. Phys. 230 (10) (2011) 4028–4050.
[49] N. Tillyaeva, Generalisation of modified Godunov scheme to arbitrary irregular meshes, Trans. Centr. Aerohydrodyn. Inst. 17 (2) (1986) 18–26.
[50] V. Kolgan, Application of the principle of minimizing the derivative to the construction of finite-difference schemes for computing discontinuous solutions of gas dynamics, J. Comput. Phys. 230 (7) (2011) 2384–2390.
[51] A. Rodionov, Complement to the "Kolgan project", J. Comput. Phys. 231 (13) (2012) 4465–4468.
[52] T.J. Barth, D.C. Jespersen, The design and application of upwind schemes on unstructured meshes, in: 27th Aerospace Sciences Meeting, 1989.

[53] V. Venkatakrishnan, Convergence to steady state solutions of the Euler equations on unstructured grids with limiters, J. Comput. Phys. 118 (1) (1995) 120–130, https://doi.org/10.1006/jcph.1995.1084.
[54] W. Li, Y. Ren, The multi-dimensional limiters for solving hyperbolic conservation laws on unstructured grids, ii: extension to high order finite volume schemes, J. Comput. Phys. 231 (11) (2012) 4053–4077.
[55] Y. Liu, W. Zhang, Accuracy preserving limiter for the high-order finite volume method on unstructured grids, Comput. Fluids 149 (2017) 88–99.
[56] C. Michalak, C. Ollivier-Gooch, Accuracy preserving limiter for the high-order accurate solution of the Euler equations, J. Comput. Phys. 228 (23) (2009) 8693–8711.
[57] A. Antoniadis, P. Tsoutsanis, D. Drikakis, Numerical accuracy in rans computations of high-lift multi-element airfoil and aircraft configurations, in: 53rd AIAA Aerospace Sciences Meeting, 0317, 2015.
[58] A. Antoniadis, P. Tsoutsanis, D. Drikakis, High-order schemes on mixed-element unstructured grids for aerodynamic flows, in: 42nd AIAA Fluid Dynamics Conference and Exhibit, 2833, 2012.
[59] A. Antoniadis, P. Tsoutsanis, I. Kokkinakis, Z. Rana, D. Drikakis, Azure: an advanced CFD software suite based on high-resolution and high-order methods, in: 53rd AIAA Aerospace Sciences Meeting, 0813, 2015.
[60] A. Antoniadis, D. Drikakis, I.W. Kokkinakis, P. Tsoutsanis, Z. Rana, High-order methods for hypersonic shock wave turbulent boundary layer interaction flow, in: 20th AIAA International Space Planes and Hypersonic Systems and Technologies Conference, 3524, 2015.
[61] P. Tsoutsanis, H. Srinivasan, Adaptive mesh refinement techniques for high-order finite-volume WENO schemes, in: ECCOMAS Congress 2016, Crete, Greece, 2016.
[62] P. Tsoutsanis, N. Simmonds, A. Gaylard, Implementation of a low-Mach number modification for high-order finite-volume schemes for arbitrary hybrid unstructured meshes, in: ECCOMAS Congress 2016, Crete, Greece, 2016.
[63] P. Tsoutsanis, D. Drikakis, Addressing the challenges of implementation of high-order finite-volume schemes for atmospheric dynamics on unstructured meshes, in: ECCOMAS Congress 2016, Crete, Greece, 2016.
[64] A. Jalali, C. Ollivier-Gooch, Higher-order finite volume solution reconstruction on highly anisotropic meshes, in: 21st AIAA Computational Fluid Dynamics Conference, 2013.
[65] M. Dumbser, M. Castro, C. Pares, E. Toro, ADER schemes on unstructured meshes for nonconservative hyperbolic systems: applications to geophysical flows, Comput. Fluids 38 (9) (2009) 1731–1748.
[66] G.W. Stewart, Matrix Algorithms, Volume 1: Basic Decompositions, Society for Industrial and Applied Mathematics SIAM, 1998.
[67] E. Toro, M. Spruce, W. Speares, Restoration of the contact surface in the HLL-Riemann solver, Shock Waves 4 (1) (1994) 25–34.
[68] A. Harten, B. Enquist, S. Osher, S.R. Chakravarthy, Uniformly high order accurate essentially non-oscillatory schemes, iii, J. Comput. Phys. 71 (2) (1987) 231–303.
[69] R.J. Spiteri, S.J. Ruuth, A new class of optimal high-order strong-stability-preserving time-stepping schemes, SIAM J. Numer. Anal. 40 (2) (2002) 469–491.
[70] D. Balsara, C.-W. Shu, Monotonicity preserving weighted essentially non-oscillatory schemes with increasingly high order of accuracy, J. Comput. Phys. 160 (2) (2000) 405–452.
[71] C.-W. Shu, S. Osher, Efficient implementation of essentially non-oscillatory shock-capturing schemes, ii, J. Comput. Phys. 83 (1) (1989) 32–78.
[72] P. Woodward, P. Colella, The numerical simulation of two-dimensional fluid flow with strong shocks, J. Comput. Phys. 54 (1) (1984) 115–173.
[73] H. Li, G. Ben-Dor, Analysis of double-Mach-reflection wave configurations with convexly curved Mach stems, Shock Waves 9 (1999) 319–326.
[74] A.N. Semenov, M.K. Berezkina, I.V. Krassovskaya, Classification of pseudo-steady shock wave reflection types, Shock Waves 22 (2012) 307–316.
[75] M. Nazarov, A. Larcher, Numerical investigation of a viscous regularization of the Euler equations by entropy viscosity, Comput. Methods Appl. Mech. Eng. 317 (2017) 128–152.
[76] C.W. Schulz-Rinner, J. Collines, H.M. Glaz, Numerical solution of the Riemann problem for two-dimensional gas dynamics, SIAM J. Sci. Comput. 7 (1993) 1394–1414.
[77] B.W. Skews, H. Kleine, Flow features resulting from shock-wave impact on a cylindrical cavity, J. Fluid Mech. 580 (2007) 481–493.



https://dspace.org/

Extended bounds limiter for high-order finite-volume schemes on unstructured meshes

Tsoutsanis, Panagiotis

2018-02-09
Elsevier
https://doi.org/10.1016/j.jcp.2018.02.009
Tsoutsanis P. (2018) Extended bounds limiter for high-order finite-volume schemes on unstructured meshes. Journal of Computational Physics, Volume 362, June 2018, pp. 69-94

Downloaded from a DSpace repository. https://dspace.org/